Politecnico di Torino

Department of Electronics and Telecommunications
School of Electronic, Telecommunications and Physics Engineering

MASTER'S DEGREE COURSE IN ELECTRONIC ENGINEERING

Development of a Portable System for Fluorescence-Based Water Contamination Detection

Supervisor:
Prof. **Guido Perrone**

Candidate:
Gabriele D'Oria

Co-supervisors:
Chiara Bellezza Prinsi
Leonardo Degl'Innocenti

A.y. 2025/2026

Abstract

Access to safe drinking water remains a major global challenge, affecting a significant portion of the world's population, particularly in low- and middle-income regions. The presence of microbiological contaminants in water supplies poses a serious threat to public health, contributing to the spread of waterborne diseases and increased mortality rates. Ensuring water quality through regular monitoring is therefore essential. However, standard microbiological assessment methods predominantly rely on laboratory techniques such as culture and molecular analysis. Although highly accurate, these approaches are often time-consuming, expensive, and dependent on specialized infrastructure, equipment, and personnel, making them unsuitable for rapid decision-making and routine implementation in resource-limited settings. In response to these limitations, there is a growing need for alternative water quality assessment strategies that are faster, more accessible, and adaptable to different environmental and socioeconomic contexts. Optical sensing techniques have proven promising, enabling rapid, non-invasive, and potentially low-cost analyses while minimizing sample preparation and operational complexity. Fluorescence-based methods are particularly attractive, as they exploit induced or intrinsic fluorescence mechanisms, for example, due to the presence of bacterial contamination. This thesis presents the development of a prototype, cost-effective, portable fluorescence instrument designed for water quality monitoring. The system is based on a miniaturized spectrometer combined with a programmable LED array, which allows for controlled optical excitation and spectral detection. The instrument is designed for battery operation, facilitating field and remote location deployment. It also integrates real-time water sample temperature monitoring and a precision LED driver circuit to ensure stable, reproducible, and well-characterized excitation conditions. Preliminary tests using fluorescent microspheres as bacterial models were conducted to validate the detection approach. Overall, the proposed system aims to bridge the gap between simplicity, portability, and analytical capability, offering a flexible and scalable platform for rapid water quality assessment.

Contents

Introduction 1

1 Theoretical introduction 3
1.1 Fluorescence . . . 3
1.1.1 Jablonski Diagram . . . 3
1.1.2 Franck-Condon Principle . . . 5
1.1.3 Fluorescence Lifetimes and Quantum Yields . . . 6
1.1.4 Fluorescence Quenching . . . 7
1.1.5 Fluorescence Spectra . . . 8
1.1.6 Factors affecting fluorescence . . . 9

2 State of the art 11
2.1 Historical Background on optical sensors . . . 11
2.2 Fluorescent optical sensors applications . . . 12
2.2.1 Smartphone-based fluorescence detection of pathogenic bacteria 12
2.2.2 Low-cost dynamic light scattering to detect *Rotavirus* particles in drinking water . . . 14

3 Preliminary experimental evaluation 16
3.1 Laboratory Measurements . . . 16
3.1.1 Lab Setup . . . 16
3.1.2 Fluorescein . . . 18
3.2 Design evaluation . . . 20
3.2.1 Simulation of 4 leds . . . 23

4 Hardware Design of the Custom PCB 30
4.1 STM32 microcontroller . . . 31
4.2 USB Type-C® . . . 33
4.2.1 USB Type-C® receptacle . . . 34
4.2.2 USB Type-C® implementation . . . 34
4.3 Power supply design . . . 36

4.3.1 Low Drop Output(LDO) . . . 37
4.3.2 Decoupling . . . 38
4.3.3 Battery charging circuitry . . . 39
4.3.4 Boost converter . . . 42
4.4 Led Driver . . . 45
4.4.1 Led Diode Driver-1 . . . 45
4.4.2 Led Diode Driver-2 . . . 50
4.4.3 Switching circuit between PWM and Howland pump . . . 52
4.4.4 Schematic of the Howland current pump . . . 57
4.4.5 Security Circuitry . . . 59
4.5 Temperature Sensing . . . 62
4.6 Compact spectrometer data acquisition . . . 65
4.7 PCB Layout . . . 68

5 Firmware configuration 71
5.1 Program flow . . . 72
5.2 Program flow of the DAC . . . 75

6 Conclusions 78

List of Figures 79

List of Tables 82

Bibliography 84

Introduction

Water management and treatment remain crucial challenges for both public health and environmental sustainability. Poor water quality can cause serious infections in humans and animals, reduce food production, and compromise ecosystem functioning and biodiversity.

In 2015, the United Nations defined the 17 Sustainable Development Goals (SDGs) as part of the 2030 Agenda for Sustainable Development. Among these, SDG 6 focuses on ensuring the availability and sustainable management of water and sanitation for all. Despite global efforts, a significant portion of the world's population still lacks access to safe drinking water, exposing millions of people to preventable waterborne diseases.

Improving the characterization and monitoring of wastewater quality is therefore essential to optimize treatment processes, identify contaminants of concern, and ensure the sustainable discharge of treated water into the environment. Wastewater quality is generally assessed through physical, chemical, and biological parameters. Physical parameters include turbidity, color, odor, solids concentration, temperature, conductivity, and pH. Chemical parameters include chemical oxygen demand, total organic carbon, nitrogen and phosphorus compounds, chlorides, sulfates, and alkalinity. Biological parameters concern the presence of indicator microorganisms, such as total coliforms, Escherichia coli, and nematodes.

Water in healthcare environments presents additional risks. Pathogens such as *Legionella* can proliferate in the warm, stagnant water of hospital plumbing systems, posing a serious threat to immunocompromised patients. Other opportunistic Gram-negative bacteria, including *Pseudomonas* and *Acinetobacter*, can colonize water systems, causing sporadic infections or localized outbreaks.

A noteworthy characteristic of many microorganisms and chemical pollutants is their ability to fluoresce when exposed to excitation sources such as LEDs or lasers. This fluorescence produces a characteristic emission spectrum, effectively serving as a "fingerprint" that enables rapid and specific identification.

In recent years, fluorescence spectroscopy has established itself as a valuable tool for water quality monitoring due to its simplicity, speed, and cost-effectiveness. The technique has been successfully applied to the detection of chemical compounds,

bacterial identification, and wastewater composition analysis. Its ability to provide rapid, continuous, and non-invasive measurements makes it particularly promising for improving water monitoring in both public and healthcare settings.
This thesis explores innovative approaches for the real-time detection of microbial contamination in water, with the aim of contributing to the development of more efficient, accessible, and sustainable monitoring strategies to support public health and environmental management.

Chapter 1

Theoretical introduction

1.1 Fluorescence

Fluorescence is a three-step physical process that allows selective and sensitive detection of components within complex biomolecular assemblies. The phenomenon is based on the absorption of a photon by a molecule (fluorophore), followed by a brief excited state period and the subsequent emission of a photon with lower energy (longer wavelength).
Critical parameters for the effectiveness of a fluorescence experiment include the Stokes shift, which facilitates the distinction between excitation and emission, the quantum yield, and the extinction coefficient. Although fluorescence is an extremely powerful tool, its effectiveness can be limited by phenomena such as photobleaching (irreversible destruction of the fluorophore), quenching (signal reduction due to molecular interactions), and sample autofluorescence[1]. Optimizing signals requires careful selection of fluorophores, the use of appropriate optical filters, and, in some cases, the employment of signal amplification techniques or ratiometric measurements.

1.1.1 Jablonski Diagram

The processes that occur between the absorption and emission of light are typically illustrated using a Jablonski diagram[1]. These diagrams often serve as the starting point for discussions of light absorption and emission and are presented in various forms to depict the different molecular processes that can occur in excited states. They are named after Professor Alexander Jablonski, who is considered the father of fluorescence spectroscopy due to his numerous contributions, including the description of concentration depolarization and the introduction of the term anisotropy to describe polarized emission from solutions.
A typical Jablonski diagram is shown in figure 1.1.

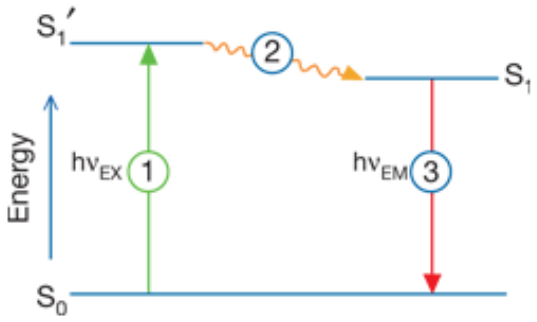

Figure 1.1: Jablonski diagram illustrating the processes involved in the creation of an excited electronic singlet state by optical absorption and subsequent emission of fluorescence[1].

Stage 1: Excitation

A photon with energy $h\nu_{\mathrm{EX}}$ from an external source, such as an incandescent lamp or a laser, is absorbed by the fluorophore, creating an excited electronic singlet state (S_1'). This absorption-based excitation differentiates fluorescence from chemiluminescence, where the excited state is instead produced through a chemical reaction.

Stage 2: Excited-State Lifetime

The excited state persists for a brief period, typically 1-10 nanoseconds. During this time, the fluorophore may undergo conformational changes and interact with its surrounding molecular environment in multiple ways. These interactions have two major consequences:

1. The energy of S_1' is partially lost, producing a relaxed singlet excited state (S_1) from which fluorescence emission occurs.

2. Not all molecules excited in Stage 1 return to the ground state (S_0) via fluorescence. Alternative pathways, such as collisional quenching, Fluorescence Resonance Energy Transfer (FRET), or intersystem crossing, can also depopulate S_1.

Stage 3: Fluorescence Emission

A photon with energy $h\nu_{\mathrm{EM}}$ is emitted, returning the fluorophore to its ground state (S_0). Because energy is partially dissipated during the excited-state lifetime, the emitted photon has a lower energy (longer wavelength) than the excitation

photon ($h\nu_{\mathrm{EX}}$). The energy or wavelength difference, ($h\nu_{\mathrm{EX}} - h\nu_{\mathrm{EM}}$), is known as the Stokes shift.
The Stokes shift is crucial for the sensitivity of fluorescence techniques, as it allows emission photons to be detected with minimal background interference, separate from excitation light. By contrast, absorption spectrophotometry requires measuring the transmitted light against the high intensity of incident light at the same wavelength.
The fluorescence quantum yield is the ratio of the number of photons emitted (Stage 3) to the number of photons absorbed (Stage 1) that quantifies the efficiency of fluorescence relative to these competing processes.

1.1.2 Franck-Condon Principle

The Franck-Condon principle is a fundamental concept in spectroscopy and quantum chemistry that explains the relative intensities of vibronic transitions. When a molecule absorbs or emits a photon with sufficient energy, changes occur simultaneously in both its electronic and vibrational energy states[2].
According to this principle, a vibronic transition is most likely when the vibrational wave functions of the initial and final states exhibit significant overlap. Since electronic transitions take place much faster than nuclear motion, the nuclei can be considered effectively stationary during the transition. Consequently, transitions are favored when there is little or no change in nuclear configuration.
This leads to the following conclusions:

1. During an electronic transition, the nuclei remain essentially stationary due to their much larger mass compared to electrons.

2. The internuclear distance does not change at the moment of photon absorption or emission.

3. The highest transition intensity occurs between vibrational states that are vertically aligned across different electronic potential energy surfaces.

4. The Franck-Condon principle therefore states that electronic transitions occur without any immediate change in the positions of the nuclei.

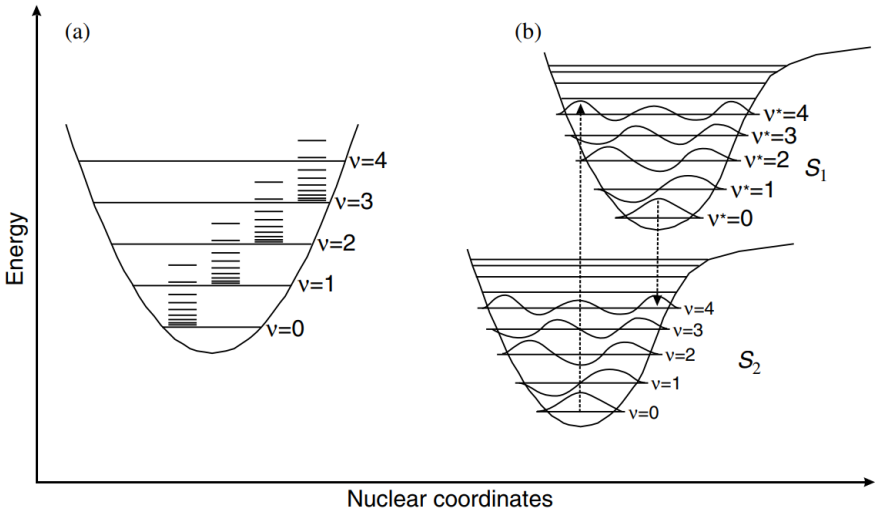

Figure 1.2: (a) Idealized potential energy curve for a diatomic molecule. In general, polyatomic molecules will have $3N - 6$ vibrational modes (ν_1, ν_2, ν_3,..), where N is the number of atoms, and will be asymmetric rotors with three different inertial axes. (b) Morse potentials for a molecule in the singlet ground state S_0 and first excited singlet state S_1 to demonstrate the Franck–Condon principle [2].

1.1.3 Fluorescence Lifetimes and Quantum Yields

Fluorescence lifetime and quantum yield are among the most important properties of a fluorophore[3]. Quantum yield is defined as the ratio of emitted photons to absorbed photons. Compounds with very high quantum yields, close to unity, such as rhodamines, produce the brightest fluorescence signals. Fluorescence lifetime is equally significant because it determines how long the fluorophore remains in the excited state. This duration influences its ability to interact with or diffuse within its environment, thereby affecting the type and amount of information that can be obtained from its emission.

The meanings of quantum yield and lifetime are best represented by a simplified Jablonski diagram (figure 1.3).

In this diagram, the individual relaxation processes leading to the relaxed S_1 state are not shown explicitly. Instead, the focus is placed on the processes responsible for the return to the ground state. In particular, we consider the radiative decay rate of the fluorophore (Γ) and the nonradiative decay rate to S_0 (k_{nr}). The fluorescence quantum yield is defined as the ratio between the number of photons emitted and the number of photons absorbed. Both Γ and k_{nr} contribute to depopulating the excited state. The fraction of fluorophores that return to the ground state through photon emission, which corresponds to the quantum yield, is given by 1.1.

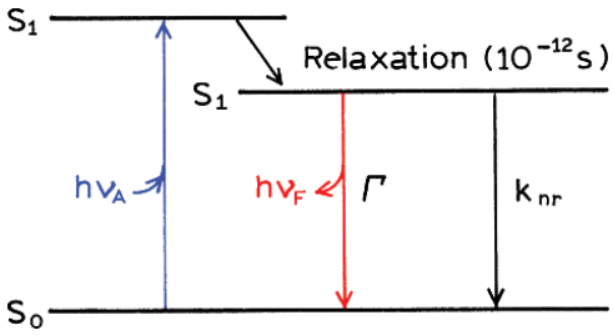

Figure 1.3: A simplified Jablonski diagram to illustrate the meaning of quantum yields and lifetimes[4].

$$Q = \frac{\Gamma}{\Gamma + k_{nr}} \tag{1.1}$$

The quantum yield approaches unity when the nonradiative decay rate is much smaller than the radiative decay rate, that is, when $k_{nr} \ll \Gamma$. However, the energy yield of fluorescence is always less than one due to Stokes losses. For simplicity, all nonradiative decay pathways are collectively represented by the single rate constant k_{nr}. The excited state lifetime is defined as the average time a molecule remains in the excited state before returning to the ground state. Fluorescence lifetimes are typically on the order of 10 ns. For the fluorophore shown in figure 1.3, the lifetime is given by 1.2.

$$\tau = \frac{1}{\Gamma + k_{nr}} \tag{1.2}$$

Fluorescence emission is inherently a stochastic process, and only a small fraction of molecules emit exactly at $t = \tau$. The lifetime represents an average time spent in the excited state.

1.1.4 Fluorescence Quenching

Fluorescence intensity can be reduced by several processes collectively known as quenching. Quenching may occur through different mechanisms. One common mechanism is collisional (or dynamic) quenching, which takes place when an excited fluorophore is deactivated through contact with another molecule in solution, called the quencher. During this diffusive encounter, the fluorophore returns to the ground state without undergoing any chemical change. For collisional quenching, the decrease in fluorescence intensity follows the Stern–Volmer equation(1.3)[4]. In

this relationship, the Stern–Volmer constant reflects how sensitive the fluorophore is to the presence of a quencher. If the fluorophore is buried within a macromolecule, it is less accessible to water-soluble quenchers, resulting in a low Stern–Volmer constant. Conversely, if the fluorophore is free in solution or exposed on the surface of a biomolecule, the constant is typically larger.

$$\frac{F_0}{F} = 1 + K[Q] = 1 + k_q \tau_0 [Q] \tag{1.3}$$

where:

F_0 = fluorescence intensity in the absence of quencher
F = fluorescence intensity in the presence of quencher
K = Stern–Volmer quenching constant
k_q = bimolecular quenching constant
τ_0 = unquenched fluorescence lifetime
$[Q]$ = quencher concentration

1.1.5 Fluorescence Spectra

The fluorescence process is inherently cyclical[1]. As long as the fluorophore is not irreversibly damaged in its excited state, commonly referred to as photobleaching, it can undergo multiple excitation and detection cycles. The ability of a single fluorophore to produce thousands of detectable photons underlies the high sensitivity of fluorescence-based detection methods.
For polyatomic molecules in solution, the discrete electronic transitions represented by $h\nu_{\mathrm{EX}}$ and $h\nu_{\mathrm{EM}}$ are broadened into continuous energy distributions, known as the fluorescence excitation spectrum and fluorescence emission spectrum (figure 1.4), respectively. The widths of these spectra are especially important when multiple fluorophores are detected simultaneously.
In dilute solutions, the fluorescence excitation spectrum of a single fluorophore typically matches its absorption spectrum. Therefore, absorption data can often serve as a surrogate for the excitation spectrum. Under the same conditions, the fluorescence emission spectrum is generally independent of the excitation wavelength because some of the excitation energy is dissipated during the excited-state lifetime. The intensity of the emitted fluorescence is proportional to the amplitude of the excitation spectrum at the chosen excitation wavelength.

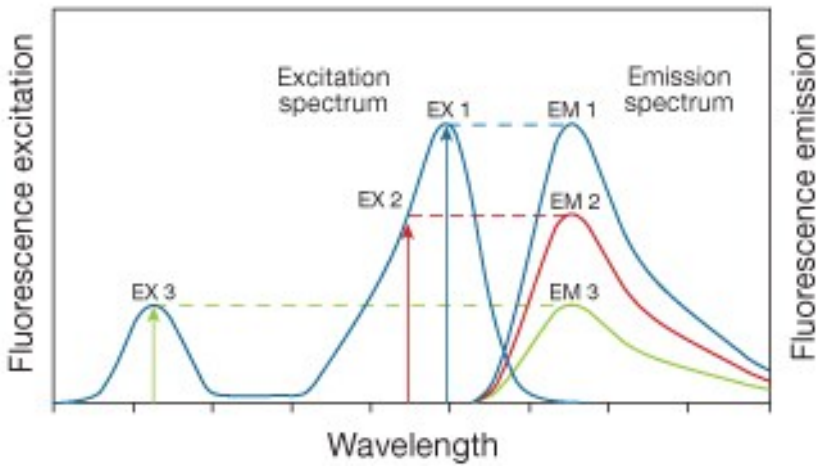

Figure 1.4: Excitation of a fluorophore at three different wavelengths (EX 1, EX 2, EX 3) does not change the emission profile but does produce variations in fluorescence emission intensity (EM 1, EM 2, EM 3) that correspond to the amplitude of the excitation spectrum[1].

1.1.6 Factors affecting fluorescence

In most cases, the fluorescence quantum yield, excited-state lifetimes, and fluorescence emission spectra remain essentially unchanged when the excitation wavelength is varied [3]. This indicates that the observed fluorescence properties are largely independent of the specific wavelength used to excite the molecule. Under ideal conditions, the fluorescence excitation spectrum should perfectly overlap with the absorption spectrum. When deviations between the two spectra are observed, they can be attributed to excitation-wavelength-dependent photoinduced processes. Let's analyze a few causes that affect fluorescence:

Non-linearity

The linear relationship between light absorption and fluorescence emission is valid only at low absorbance values. As the concentration of the fluorophore increases, this relationship becomes non-linear due to effects like incomplete penetration of the excitation light, particularly in right-angle detection setups. This causes reduced emission detection from the inner regions of the sample.
When high concentrations are necessary, for instance in enzymatic assays involving NADH (nicotinamide adenine dinucleotide in its reduced form, a coenzyme that absorbs at 340 nm and is commonly used to monitor enzymatic reactions), the linear range can be extended using microcuvettes with minimal sensitivity loss. In practice, non-linearity from absorption is negligible for solutions with transmittance

greater than 95% at the wavelength of interest. Instrumental factors, such as signal amplification and display systems, can also introduce non-linear behavior.

Temperature Effects

Fluorescence is influenced by temperature because it affects the viscosity of the medium and, consequently, the frequency of collisions between the fluorophore and solvent molecules. Many fluorophores exhibit temperature-dependent fluorescence intensity. To ensure accurate measurements, thermostatic cell holders are recommended. If measurements are taken at room temperature, samples should be allowed sufficient time to equilibrate after any heating or cooling steps.

pH Effects

Fluorescence intensity and spectral properties are highly sensitive to pH. Even minor pH changes can significantly alter fluorescence, making precise pH control essential. Buffers specified in assay protocols should not be modified without careful evaluation.
For example, phenolic compounds are fluorescent under neutral or acidic conditions but lose fluorescence in basic media due to phenate ion formation. Similarly, 5-hydroxyindoles like serotonin can exhibit large emission wavelength shifts with pH changes, even if their absorption spectra remain unchanged.

Inner-Filter Effects

Inner-filter effects occur when other substances in the sample absorb excitation or emission light, reducing observed fluorescence intensity. At high concentrations, this may be caused by the fluorophore itself, but more often it results from other absorbing species in complex samples, such as tissue or urine extracts. Proper sample preparation and extraction are crucial to remove interfering compounds and ensure consistency with standards.

Quenching

Fluorescence quenching refers to the reduction of fluorescence intensity due to specific interactions between the excited fluorophore and its environment. Though relatively uncommon, quenching is chemically specific and well-documented. A classic example is the quenching of quinine fluorescence by halide ions, even though quinine's absorption spectrum remains unchanged under different acidic conditions.

Chapter 2

State of the art

2.1 Historical Background on optical sensors

Optical sensors represent one of the oldest and most versatile technologies in the field of physical and chemical detection. The idea of using light as a measurement tool dates back to the 19th century, when Sir **Frederick William Herschel** discovered infrared in 1800 and began exploring its potential for temperature measurement. In the following decades, optics became established as a tool for precise measurements, with the development of photometers, spectroscopes, and photoelectric detectors, which allowed the conversion of light signals into quantifiable information. In the 1960s and 1970s, with the advent of lasers and optical fibers, optical sensors underwent a significant transformation. Coherent light emission and light guidance in fibers enabled the development of sensors that were more compact, sensitive, and resistant to electromagnetic interference compared to traditional electrical sensors. These innovations paved the way for systems capable of measuring physical parameters such as temperature, pressure, mechanical strain, and chemical concentration with high precision and at a distance.

Among the different types of optical sensors, those based on fluorescence have gained particular importance due to their high sensitivity and specificity.
Their operating principle is based on the absorption of light by a fluorescent molecule (fluorophore) and the subsequent emission of light at a longer wavelength. Variations in intensity, lifetime, or emission spectrum can be correlated with environmental or chemical parameters such as pH, oxygen, metal ions, or biomolecules. The first fluorescence sensors date back to the 1960s, when systems for biological and chemical monitoring in the laboratory were developed, using organic dyes and natural fluorophores. Although the phenomenon of fluorescence was inadvertently observed much earlier by Sir Frederick William Herschel in 1845 while observing

tonic water (a quinine solution) in sunlight [4].
In the 1970s, with the advancement and development of LEDs and the first more compact and portable photoelectric sensors, it became possible to open the way to applications for studying and measuring pH, dissolved oxygen, and metal ion concentration, although still with low efficiency and limited wavelength emission.

2.2 Fluorescent optical sensors applications

At present, fluorescent sensors are used in a wide range of fields, including food, environmental, healthcare, and industrial applications.
Numerous studies in the literature report the use of fluorescent sensors for the detection of various organic and inorganic species. In particular, aptamer-based sensors (short synthetic DNA or RNA sequences capable of recognizing and binding a molecular target with high specificity and affinity) have achieved significant progress through integration with nanomaterials such as quantum dots, plasmonic nanoparticles, and molecularly imprinted polymers (MIPs), which enhance sensitivity, stability, and portability. In parallel, the emergence of new fluorophores, such as aggregation-induced emission (AIE) luminogens, has overcome the limitations of traditional dyes and enabled the development of solid-state sensors for the detection of toxic ions and heavy metals.
Alongside these selective analyte-recognition approaches, many studies also report the use of non-functionalized fluorescent systems, such as fluorescent beads, as reference standards for instrument calibration. These materials are typically deposited on a substrate and analyzed by optical or fluorescence microscopy, allowing verification of optical performance and measurement reproducibility. Although effective for instrumental quality control, these approaches are often limited to static, laboratory-based measurement configurations and show reduced adaptability to dynamic or portable sensing systems.

The following sections present a review of selected literature examples illustrating recent advances and applications of fluorescent optical sensors.

2.2.1 Smartphone-based fluorescence detection of pathogenic bacteria

A representative example of the use of unfunctionalized fluorescent beads is reported in a study in which these microspheres were employed as reference standards to evaluate the performance of a portable smartphone-based fluorescence microscopy system, figure 2.1. In this work, the beads played a key role in the initial characterization phase of the device, enabling assessment of its accuracy, precision,

and dynamic detection range prior to application to real biological samples[5]. Dilution series with concentrations ranging from 10^2 to 10^8 beads/µL in ultrapure water were prepared; aliquots of each solution were deposited onto glass slides and analyzed under controlled conditions. The comparison between the microsphere counts obtained with the portable system and those measured using a conventional benchtop microscope showed excellent agreement, confirming the reliability of the measurements. The use of fluorescent beads demonstrated that the system possessed sufficient sensitivity and resolution for the detection of single micrometric entities, highlighting how these materials, despite lacking specific functionalization, represent effective tools for the calibration and validation of sensing platforms, even in compact and potentially portable configurations, although not yet suitable for in situ, real-time, continuous monitoring.
Building on the characterization with beads, the device was subsequently applied to the detection of real pathogenic bacteria in order to evaluate its performance under more complex biological conditions. In particular, *Cronobacter sakazakii* and *Staphylococcus aureus* were cultured, fixed onto glass slides, and fluorescently labeled either with the nucleic acid stain SYTO 9 or with specific PNA probes (the universal EUB338 probe and the *Cronobacter* species-specific CRONO probe). The images acquired with the smartphone-based system were compared with those obtained using a conventional benchtop fluorescence microscope, showing clear visualization of the labeled bacteria and comparable sensitivity within the investigated concentration range. Furthermore, to simulate real matrices and verify system specificity, experiments were conducted on mixed cultures and artificially contaminated powdered infant formula samples, demonstrating the device's ability to selectively identify the target microorganism even in the presence of a complex background [5].

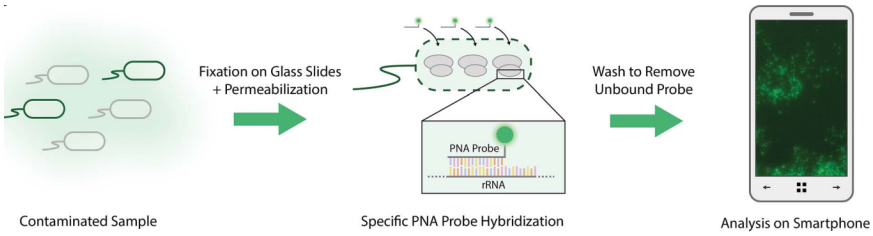

Figure 2.1: Schematic of bacterial detection: Bacteria are fixed on glass slides, permeabilized to allow entry of a PNA probe labeled with Alexa Fluor 488, which binds specific rRNA regions. After washing, only the targeted bacteria remain fluorescent and can be imaged with the smartphone microscope[5].

2.2.2 Low-cost dynamic light scattering to detect *Rotavirus* particles in drinking water

In this study, the researchers developed a simple, low-cost instrumentation system suitable for implementation in resource-limited settings[6]. The setup, illustrated in Figure 2.2, employs a 5 mW, 532 nm laser focused into a water sample contained in a cuvette using a plano-convex lens. Scattered light is collected perpendicularly with a cleaved SMF-28 optical fiber and measured using a photodiode with a custom amplifier. The intensity signals are acquired via a microcontroller.
To characterize the method, live attenuated *Rotavirus* from the Rotarix oral vaccine was used. The approach relies on the scattering of light by particles passing through the laser's focal point. The collected signal is first corrected for large-scale drifts. A peak detection algorithm is then applied to identify events corresponding to particles crossing the focal point.
The algorithm begins by calculating the base noise level, defined as the standard deviation (σ) of the pure water signal (Figure 2.3a, black trace). Deviations from this baseline are considered potential particle scattering events. Points exceeding $\pm 4\sigma$ are flagged as candidate events, which may correspond to single or multiple particles entering or exiting the focal region. The duration of the signal above or below the threshold is also taken into account. For an event to qualify as a particle detection, multiple consecutive points must exceed the threshold. When two events occur in close succession, a minimum time interval threshold (τ_{th}) is applied, defined as the mean duration of individual events in which the signal crosses zero. Testing this algorithm on pure water data produced no false detections.
The method was then applied to detect live attenuated rotavirus particles. Several scattering events corresponding to viral detection are shown in Figure 2.3a alongside the baseline pure water signal. A zoomed-in view (Figure 2.3b) highlights individual detection events. Figure 2.3c shows the total number of detected events for different virus concentrations ranging from 125 kU/mL to 4 kU/mL. No events were observed in pure water, while all tested virus concentrations produced detectable scattering events, demonstrating the sensitivity of the system to rotavirus particles[6].

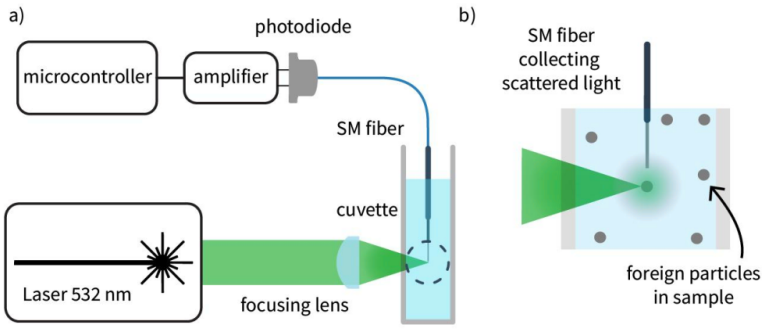

Figure 2.2: a)Schematic of the DLS-based system used in the experiments. b)Detail showing fiber collecting scattered light[6].

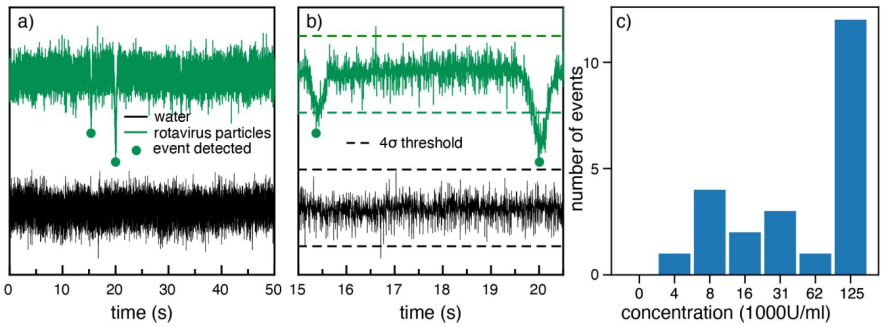

Figure 2.3: a)Signals of water. b)Zoomed-in version of a). c)Number of events detected by our system in 10 min for different concentrations of virus particles[6].

Chapter 3

Preliminary experimental evaluation

3.1 Laboratory Measurements

The initial phase of this study involves analyzing the phenomenon of fluorescence using a specially designed laboratory setup, observing key characteristics such as emission intensity, wavelength, and quantum efficiency, with the aim of understanding the mechanisms governing the behavior of fluorescent materials.

3.1.1 Lab Setup

The laboratory setup used consists of a LED driver (LEDD1B, Thorlabs [7], figure 3.2) with a mounted LED (M450LP2, Thorlabs [8], figure 3.3), a spectrometer (AvaSpec-3648, Avantes [9], figure 3.4), a cuvette holder, and a standard multimode fiber optic cable.

The spectrometer is the most important piece of hardware in the experiment: it captures the spectrum of the incoming light (ranging from 200 nm to 1100 nm) through a fiber optic cable and transmits it to the PC, where acquisition software displays the spectrum on the screen and allows it to be saved.
The optical fiber, attached to one side of the cuvette holder, collects the light inside the cuvette.
The unused sides of the cuvette holder, including the top, should be closed with caps to prevent any light interference from outside.

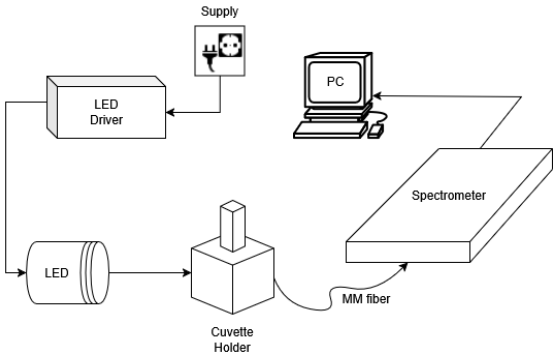

Figure 3.1: Illustration of the measurement concept.

Figure 3.2: T-Cube LED Driver [7].

Figure 3.3: M450LP2 mounted LED [8].

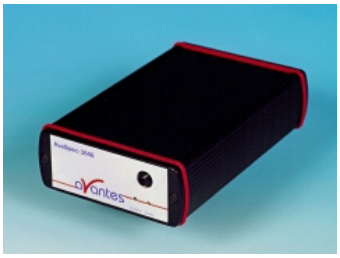

Figure 3.4: Avantes Spectrometer LED [9].

3.1.2 Fluorescein

Sodium fluorescein (Uranine) was selected as the tracer due to its polar nature, which ensures easy solubility in aqueous media. The dye is widely available, inexpensive, and of consistent quality, which facilitates reproducibility in experiments. For measurements, changes in the protonation state of the sodium fluorescein fluorophore alter its electronic structure, producing a measurable variation in the emitted light.
The stock solution was prepared by dissolving 1.1 g of fluorescein in 200 mL of distilled water, thus obtaining a solution with a known concentration. Subsequent dilutions were carried out by removing 150 mL of solution at each step and replacing it with 150 mL of water, keeping the total volume constant. This procedure ensured a gradual and controlled decrease in the fluorophore concentration.
Excitation was carried out using a LED with a central wavelength of approximately 450 nm, consistent with the absorption band of fluorescein. The characteristic emission of fluorescein is instead observed with a maximum around 530 nm, highlighting the emission spectra.
As shown in figure 3.5 and 3.6, a progressive decrease in fluorescence intensity is observed with increasing dilution, consistent with the reduction in fluorophore concentration and with the linear dependence of emission intensity on concentration at low concentrations. At higher dilution levels, the fluorescein emission signal becomes comparable to the instrumental background noise until it disappears, leaving the blue LED emission spectrum centered at 450 nm as the dominant contribution.
A quadratic interpolation (figure 3.7) $y = at^2 + bt + c$ of the line in the figure 3.6 was used to estimate the intermediate values of the experimental data more accurately and to identify any nonlinear trends.

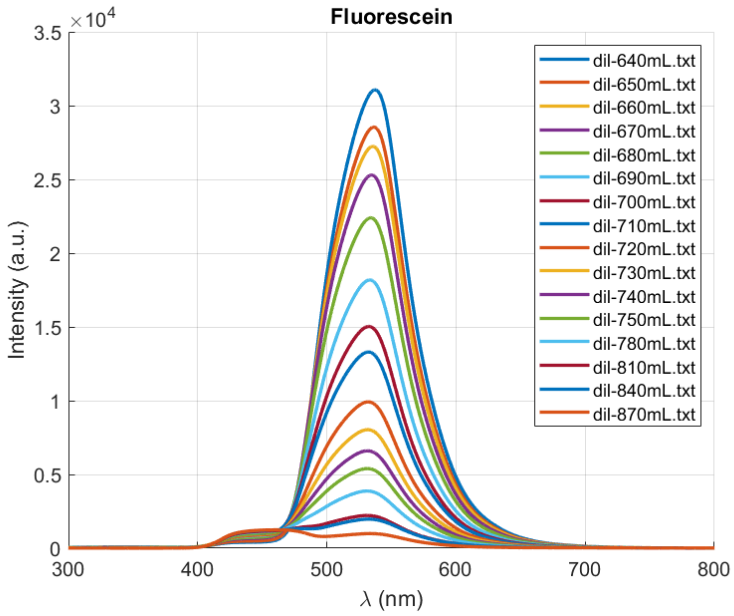

Figure 3.5: Spectra captured by the laboratory spectrometer.

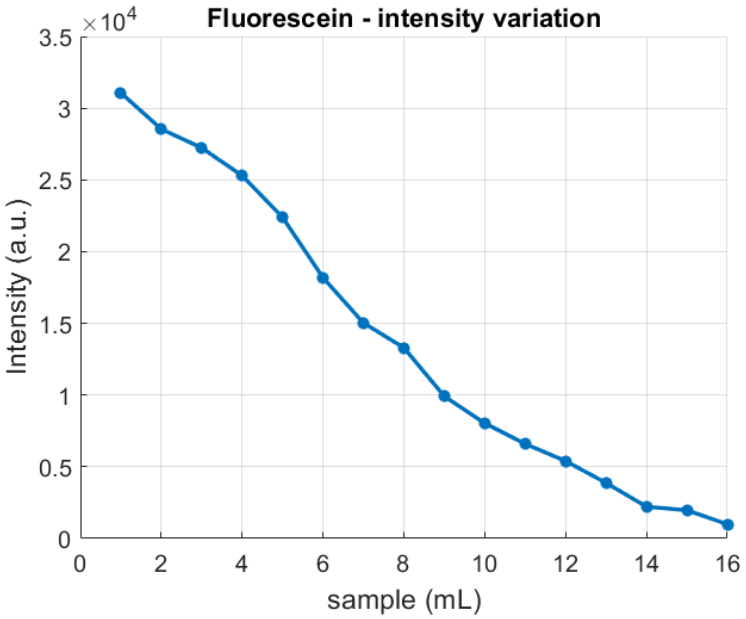

Figure 3.6: Illustration of the intensity variation.

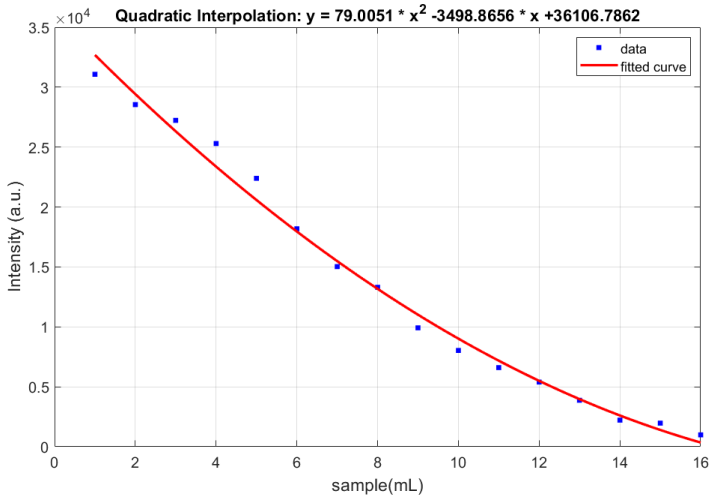

Figure 3.7: Quadratic interpolation.

3.2 Design evaluation

To enable the extension of the methodology developed in the benchtop setup toward a broader implementation, potentially applicable even in resource-limited settings, a simple and cost-effective instrumental configuration was considered. This configuration involves the use of four excitation LEDs operating at different wavelengths and a low-cost miniaturized spectrometer.
As illustrated in the figure 3.8, the design concept consists of positioning the four LEDs in front of the sample, while the Adafruit mini-spectrometer AS7341[10] is placed at 90° relative to the illumination direction. This configuration reduces the detection of direct or scattered excitation light, which can overwhelm the weaker fluorescent signal. Fluorescence emission is largely isotropic, allowing effective signal collection perpendicular to the excitation path. Additionally, the 90° geometry reduces specular reflections from the sample surface, improving measurement accuracy and signal-to-noise ratio. Consequently, this perpendicular setup is a standard practice in fluorescence spectroscopy for maximizing sensitivity and selectivity. So, the resulting spectra will subsequently be analyzed to estimate the concentration of particles present in the water.
A custom PCB was also designed, incorporating a microcontroller (MCU) dedicated to the handling of the LED matrix and to the acquisition of data from the mini-spectrometer. This solution enables the integration of excitation control and optical signal readout into a single compact system.
Four LEDs with different wavelengths and a luminous flux suitable for exciting the samples under analysis were considered. To assess the suitability of LEDs

with comparable characteristics for fluorescence applications, preliminary tests were performed using the Thorlabs M450LP2[8]. The results demonstrated that its performance was adequate for the intended application; consequently, it was adopted as the reference device for subsequent design choices. The selected LEDs are reported in table 3.1.
The choice of wavelengths was guided by the need to excite two types of fluorescent beads available in the laboratory, with excitation peaks at 470 nm and 520 nm, respectively. The beads are polymeric microspheres, typically micrometer-sized, incorporating fluorophores with well-defined spectral characteristics. They are commonly used as reference samples or models for the calibration and validation of optical systems and biosensors. Furthermore, selecting LEDs operating in the 365 nm-520 nm range broadens the available excitation spectrum, making the system potentially suitable for the excitation of real bacteria, which exhibit auto-fluorescence in specific regions of the UV-visible spectrum. Figure 3.9 and 3.10 illustrates the two SMD LEDs employed in the LED matrix configuration.

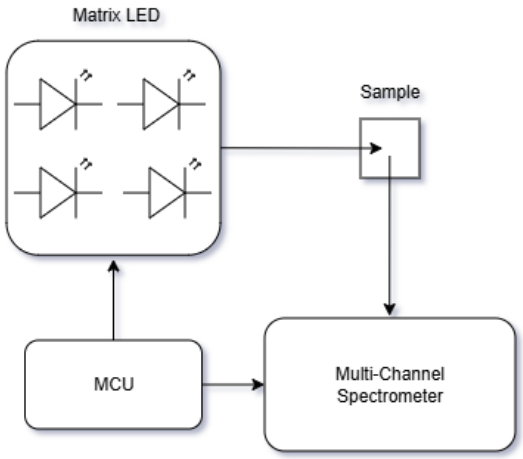

Figure 3.8: Illustration of the measurement concept.

Type	Manufacturer	Peak wavelength	Luminous flux	Forward current	Forward voltage
Ultraviolet	Wurth Elektronik[11]	365 nm	1,000 mW	500 mA	3.8 V
Ultraviolet	Wurth Elektronik[11]	395 nm	1,100 mW	500 mA	3.5 V
Blue	Lumileds[12]	460 nm-485 nm	41 lm	350 mA	2.95 V
Green	Lumileds[12]	520 nm-540 nm	102 lm	350 mA	2.95 V

Table 3.1: LED characteristics.

Figure 3.9: UV Led SMD Wurth Elektronik[11].

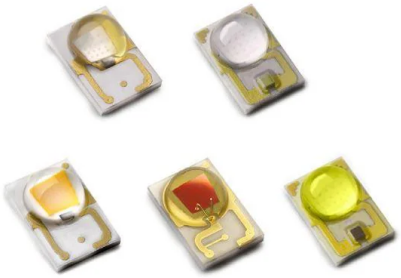

Figure 3.10: LUXEON Rebel Color single color Led SMD [12].

3.2.1 Simulation of 4 LEDs

The geometric arrangement of the LEDs plays a crucial role in ensuring uniform and effective illumination of the sample. To this end, two possible configurations were analyzed: a square arrangement (LED matrix), in which the LEDs are positioned at the vertices of a square around the optical axis, and a horizontal linear arrangement (LED array). Comparing these two configurations makes it possible to evaluate which solution ensures greater beam homogeneity, reduced mutual interference between sources, and a more stable and reproducible spectral response of the measurement system.
To compare the configuration of the LEDs[13], the irradiance equation (3.1) was used to plot in MATLAB the optical behavior of each of the four individual LEDs and to calculate the total irradiance when all four LEDs were turned on simultaneously. For this purpose, an inter-LED distance of 0.5 cm and a distance of approximately 1.3 cm between the LEDs and the sample were considered.

$$E_k(x,y) = \frac{4\,\Phi_k}{\pi\left(4h^2 + \frac{w_k^2}{100}\right)} \cdot \frac{h^4}{\left(h^2 + (x-x_k)^2 + (y-y_k)^2\right)^2} \tag{3.1}$$

Where:

- Φ_k : power of LED k (mW)
- h : LED-to-sample distance (cm)
- w_k : diameter of LED k (mm)
- (x_k, y_k) : position of LED k
- $R_k^2 = (x-x_k)^2 + (y-y_k)^2$: radial distance from the LED

The total irradiance is the sum of the contributions from all LEDs:

$$E_{\text{tot}}(x,y) = \sum_{k=1}^{4} E_k(x,y) \tag{3.2}$$

In the first phase, the LED array configuration was analyzed, as shown in figure 3.11, which reports the irradiance of the individual LEDs. Subsequently, the light propagation from the LEDs onto the cuvette containing the sample was simulated, taking into account that standard cuvette have a width of approximately 1.1 cm. The plot in figure 3.12 clearly shows that LEDs 1 and 4 are partially outside the cuvette, indicating that the initial array configuration does not ensure uniform illumination of the sample. To optimize light distribution, a LED matrix configuration was adopted. As shown in the figure 3.14, the total irradiance of the four LEDs in

the new configuration uniformly covers the entire area of the cuvette. Figure 3.13 shows the irradiance of single LEDs.
For a more detailed evaluation, the combined irradiance of LEDs (figure 3.15, 3.16 and 3.17) switched on in pairs was also plotted, allowing a comparison between the partial light distribution and the total irradiance achieved by all four LEDs operating simultaneously.

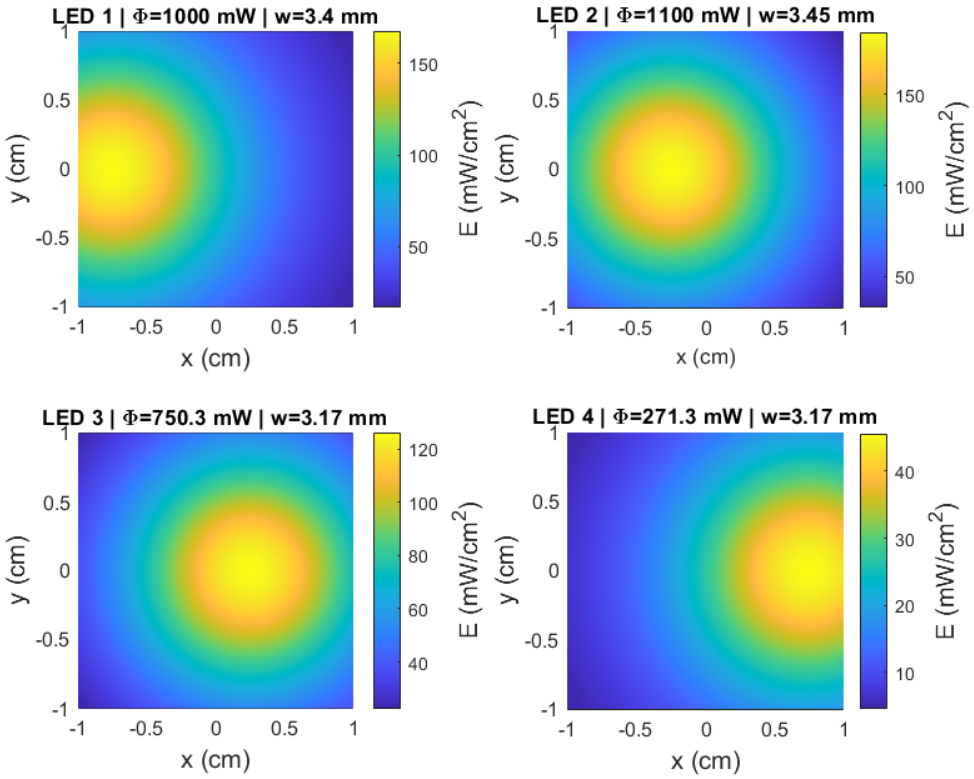

Figure 3.11: Irradiance of single LEDs (LED array).

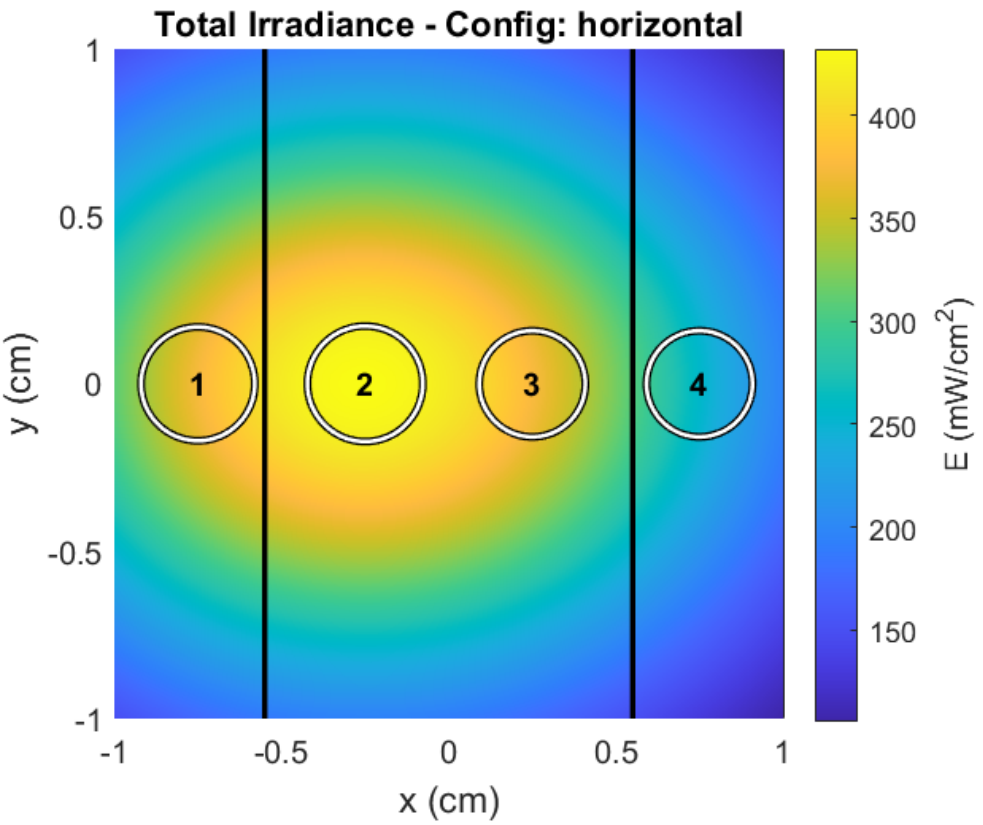

Figure 3.12: Total irradiance of the LED array (the circles represent the positions of the various LEDs, while the vertical lines the position of the cuvette).

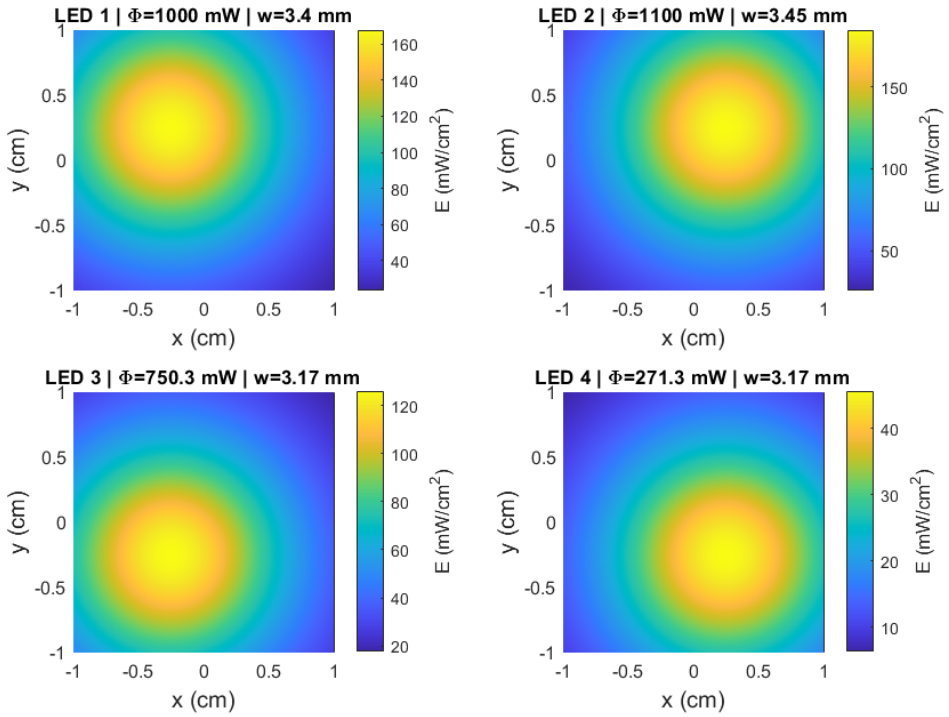

Figure 3.13: Irradiance of single leds (LED matrix).

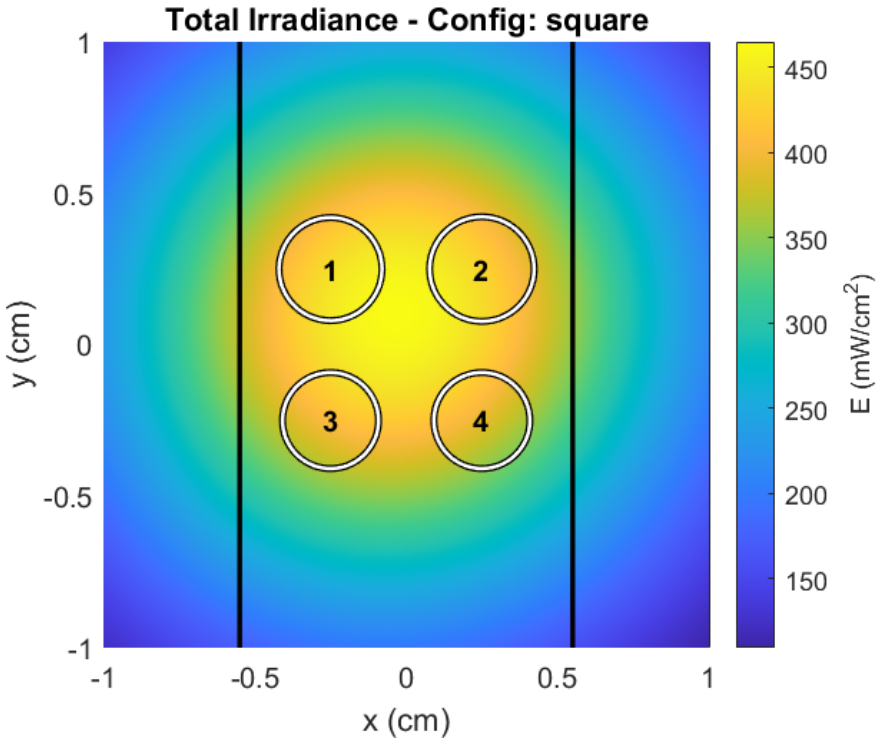

Figure 3.14: Total irradiance of the LED matrix (the circles represent the positions of the various LEDs, while the vertical lines the position of the cuvette).

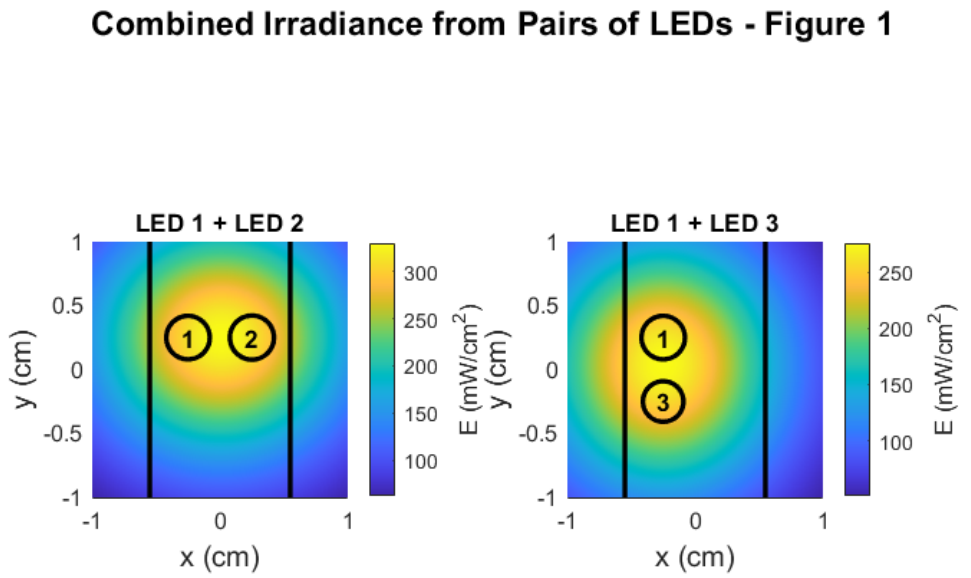

Figure 3.15: Combined irradiance of the LED matrix(LED 1+LED2; LED1+LED3).

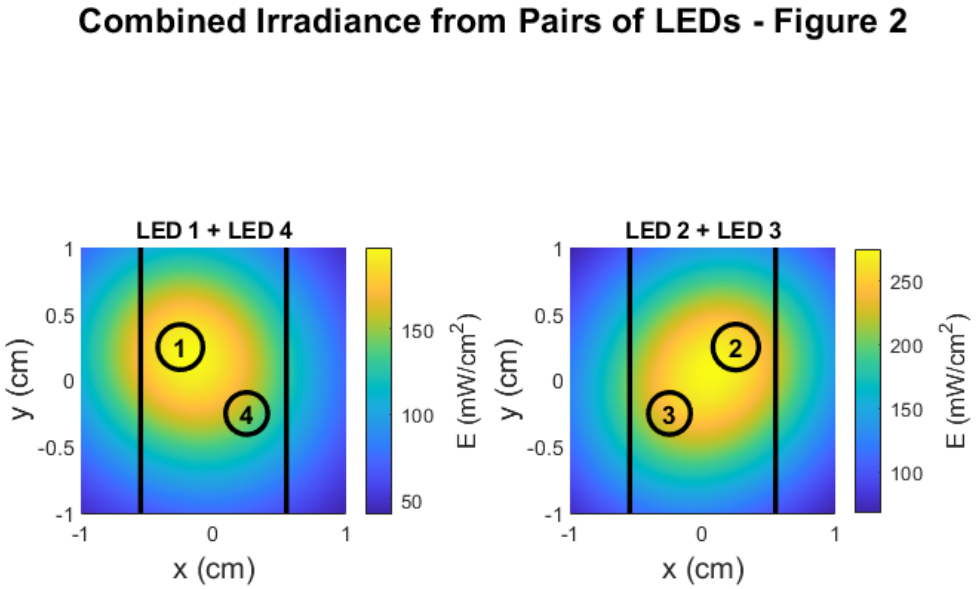

Figure 3.16: Combined irradiance of the LED matrix(LED 1+LED4; LED2+LED3).

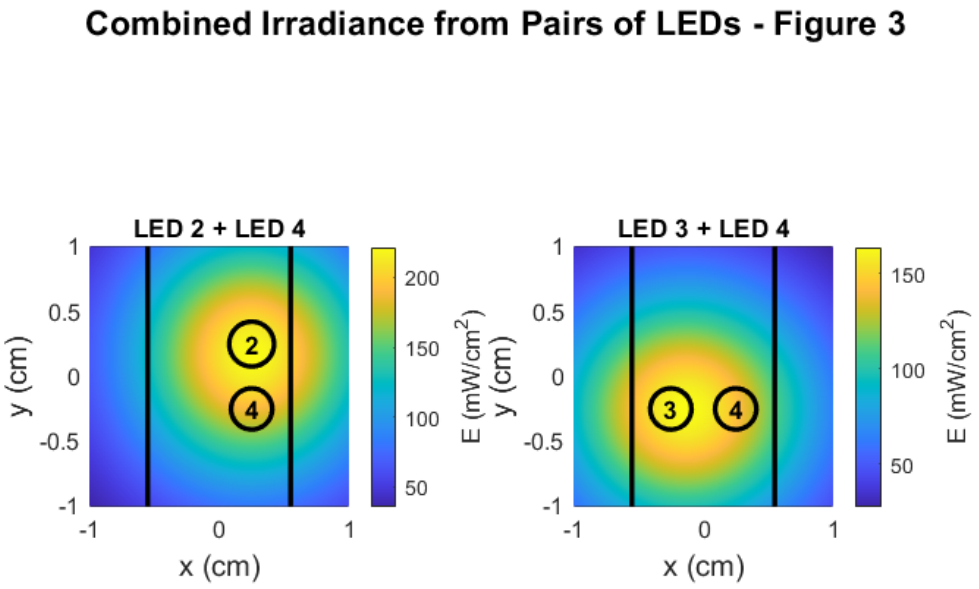

Figure 3.17: Combined irradiance of the LED matrix(LED 2+LED4; LED3+LED4).

Chapter 4

Hardware Design of the Custom PCB

A PCB prototype was developed to assess the feasibility of the proposed measurement scheme in a real-device environment, rather than relying solely on laboratory simulations. The design adopts a four-layer PCB stack-up, illustrated in the figure, with an overall thickness of 1.6 mm and manufactured using standard FR4 material. The top layer hosts all the electronic components, while the remaining three layers are primarily dedicated to solid planes (ground and power) in order to reduce parasitic impedance and improve trace integrity.

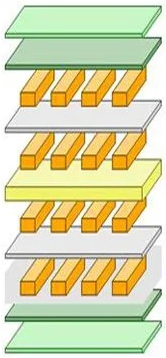

4 Layers PCB Stackup (Thickness 63mil/1.6mm)

4 Layers PCB Stackup (Default)	Layer Name	Type	Material	Thickness (mm)	Thickness (mil)	Dielectric Material	Dielectric Constant
	Top Overlay 1	Overlay	Overlay				
	Top Solder 1	Solder Mask Oil	Surface Material	0.01016	0.40	Solder Resist	3.5
	Top Layer	Signal	Copper	0.035	1.38		
	Dielectric 1	Dielectric	Prepreg	0.122	4.80		4.2
	Signal Layer 1	Signal	Copper	0.035	1.38		
	Dielectric 2	Dielectric	Core	1.15	45.28	FR4	4.2
	Signal Layer 2	Signal	Copper	0.035	1.38		
	Dielectric 3	Dielectric	Prepreg	0.122	4.80		4.2
	Bottom Layer	Signal	Copper	0.035	1.38		
	Bottom Solder 1	Solder Mask Oil	Surface Material	0.01016	0.40	Solder Resist	3.5
	Bottom Overlay	Overlay					

Figure 4.1: Four-layer PCB stack-up [14].

Choosing a **4-layer PCB** over a 2-layer board is a strategic decision because it offers numerous key advantages that improve **performance**, **reliability**, and **design compactness**. This advanced structure is ideal for complex or high-density circuits, providing benefits that a 2-layer board simply cannot match. The following outlines the key advantages of a 4-layer PCB.

1. Superior Signal Integrity

With two additional layers, high-speed signals can be separated from power and ground planes, reducing noise and distortion. This ensures cleaner, more stable signals—essential for high-frequency designs.

2. Reduced Interference and Crosstalk

A dedicated ground plane allows signals to return without radiating noise, significantly lowering **electromagnetic interference (EMI)** and crosstalk between traces. This enhances overall device stability and reliability.

3. Improved Thermal Management

Internal copper layers help distribute heat evenly, reducing the risk of overheating and protecting sensitive components. This is especially important in high-power or densely packed circuits.

4. Higher Routing Density

More layers provide more routing options without increasing board size. This allows integration of additional features and components in an organized and manufacturable way.

5. Compact and Optimized Design

Routing signals across multiple layers enables smaller, sleeker boards ideal for modern electronics such as smartphones, tablets, and wearable devices without compromising performance.

4.1 STM32 microcontroller

The heart of the PCB is the STM32WB55RG microcontroller[15] (VFQFPN68 package) from STMicroelectronics, which serves as the main processing unit. The STM32WB55RG is a low-power multiprotocol microcontroller designed for advanced wireless applications. It integrates a 32-bit Arm® Cortex®-M4 core running up

to 64 MHz, featuring a single-precision FPU and DSP instructions, alongside a dedicated Cortex®-M0+ for real-time radio protocol management. The device includes a radio compliant with Bluetooth® Low Energy 5.4 and IEEE 802.15.4-2011, high-performance memory with up to 1 MB Flash and 256 kB SRAM, and a Quad-SPI interface with XIP support. Security features include dual AES engines, PKA, RNG, customer key storage, and memory protection, with portions exclusively accessible by the Cortex-M0+. The microcontroller provides a 12-bit ADC, ultra-low-power comparators, advanced timers, a low-power RTC, up to 18 capacitive sensing channels, and an integrated LCD driver up to 8x40 segments. Communication interfaces include USART, LPUART, I²C, SPI, SAI, USB 2.0 FS, and Quad-SPI. Power supply ranges from 1.71 V to 3.6 V with advanced low-power management and an integrated SMPS with automatic bypass, along with a VBAT backup for RTC and oscillator operation without the main VDD. The STM32WB55RG is available in packages up to 129 pins, making it ideal for IoT and smart wireless applications requiring high performance, low power, and advanced security. Figure 4.2 shows the schematic in KiCad of the MCU that manages the following tasks:

- Battery-charging circuitry
- Led diode Driver
- Temperature sensing
- Mini-spectrometer data acquisition

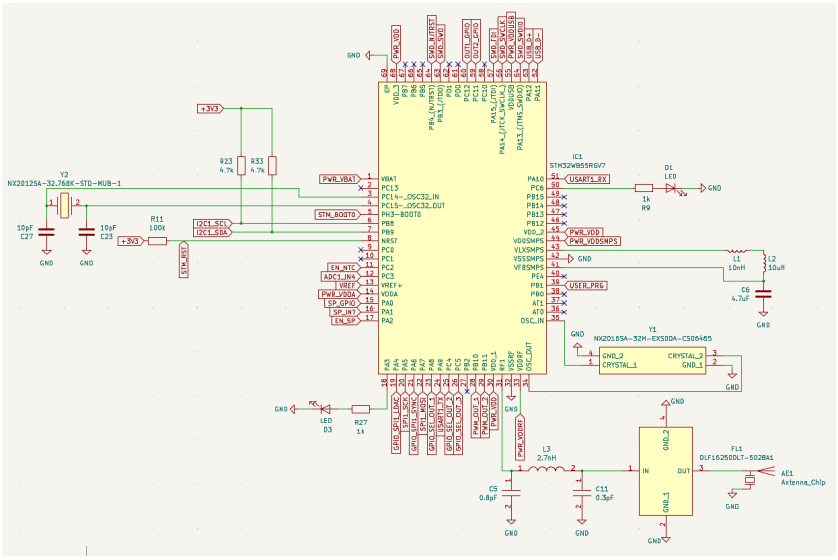

Figure 4.2: Schematic in KiCad of the MCU.

4.2 USB Type-C®

USB has evolved from a simple data interface with limited power capability into a primary power source combined with high-speed data transfer[16]. The introduction of USB Type-C® and USB Power Delivery (PD) 2.0 (with version 3.0 now widely adopted) has further accelerated this transition. However, careful consideration is required to select the most cost-effective solution for a given application, as USB Type-C® and USB PD support multiple power levels.
For instance, USB Type-C® alone can deliver up to 5 V at 3 A (15 W), whereas USB Type-C combined with USB PD enables various power profiles up to 20 V at 5 A (100 W). The trade-off is that implementing USB PD increases design complexity and raises the Bill of Materials (BOM) cost.
With notable foresight, the original USB designers ensured that the interface could carry both data and power, allowing low-power peripherals to draw energy directly from the host device. Today, billions of electronic devices feature a USB connection, and the technology has expanded far beyond its original role as a computer peripheral interface.
This remarkable expansion has also introduced greater complexity, driven by the proliferation of connector types, bandwidth options, and power levels—ranging from the original 5 V at 100 mA to the current 20 V at 5 A.
Fortunately, the landscape is becoming more streamlined. New designs increasingly adopt USB Type-C specifications 1.0, 2.0, 3.0, or 3.1 for communication, and when higher power is required, USB PD 2.0 or 3.0 power protocols are implemented. The terminology commonly used for USB Type-C system® is:

- **Source**: A port power role. Port exposing R_p on CC pins, and providing power over VBUS (5 V to 20 V and up to 5 A), most commonly a Host or Hub downstream-facing port.

- **Sink**: A port power role. Port exposing R_d (Pull down resistor) on CC pins and consuming power from VBUS (5 V to 20 V and up to 5 A), most commonly a device (such as a legacy Type-B port).

- **Dual-role power (DRP) port**: A port that can play source or sink power roles, reversible dynamically.

- **Downstream-facing port (DFP)**: A port data role. A USB port at higher level of USB tree, such as a USB host or a hub expansion.

- **Upstream-facing port (UFP)**: A port data role. A USB port at lower level of USB tree, such as a USB device or a hub master port.

4.2.1 USB Type-C® receptacle

It is not mandatory to implement or support all the advanced features defined in the USB Type-C and Power Delivery specifications. The required functions to support are:

- Cable attach and detach detection
- Plug orientation/cable twist detection
- USB 2.0 connection

The 24-pin USB Type-C® (figure 4.3) connector includes:

Symmetric connections

- USB 2.0 differential pairs (D+/D-)
- Power pins: VBUS and GND

Asymmetric connections

- Two sets of TX/RX signal paths that support USB 3.1 data speeds
- Configuration channels (CC lines) that handle discovery, configuration, and management of USB Type-C® Power Delivery features
- Two sideband use signals (SBU lines) for analog audio modes or alternate modes

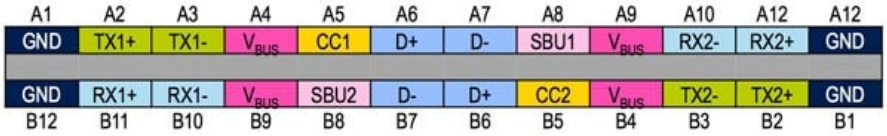

Figure 4.3: USB Type-C® connector pins[16].

4.2.2 USB Type-C® implementation

For this design, a USB Type-C®(1.2) port without USB PD was chosen, providing a solid maximum of 5 V at 3 A (15 W). The Texas Instruments TUSB320 chip was selected for the USB Type-C® implementation.
The TUSB320 is a USB Type-C® port controller that manages the configuration channel (CC) logic[17]. It detects cable connection and disconnection, orientation, port role, and current mode (default, medium, or high). The device can operate as a downstream-facing port (DFP), upstream-facing port (UFP), or dual-role port

(DRP), with VBUS detection to confirm attachment. It supports a wide voltage range, low power consumption, and is available in both commercial and industrial temperature grades.
The TUSB320 device has been configured in UFP mode by pulling the PORT pin low to GND. In UFP mode, the device continuously presents pull-down resistors (R_d) on both CC pins. It monitors the CC pins to detect the voltage level corresponding to the Type-C current advertisement provided by the connected DFP. The CC pins are debounced, and the device waits for VBUS detection before completing a successful attachment.
As a UFP, the TUSB320 detects the advertised current level from the DFP and communicates this information to the system through the OUT1 and OUT2 GPIO pins, which are connected to the MCU. The table 4.2 lists the output pin configurations for OUT1 and OUT2. GPIO mode is configured by leaving the ADDR pin unconnected. OUT3 is used to detect an audio accessory; however, since this function is not required in this project, the OUT3 pin is left unconnected.
The VBUS_DET pin must be connected to VBUS on the Type-C connector through a 900 kΩ resistor. This high value resistor protects the TUSB320 device from the maximum possible VBUS voltage in current systems. Together with the internal pull down resistor, it ensures that the voltage seen by the device remains within the recommended range.
According to the USB 2.0 specification, when the TUSB320 operates in UFP mode, a bulk capacitance between 1 µF and 10 µF is required. In this design, two capacitors were selected: 100 nF and 4.7 µF.
The figure 4.4 shows the designed USB Type-C® schematic. Note that a very low-capacitance ESD protection device has been used on the $D+$ and $D-$ signal lines.

OUT1	**OUT2**	**Advertisement**
H	H	Default Current in Unattached State
H	L	Default Current in Attached State
L	H	Medium Current (1.5 A) in Attached State
L	L	High Current (3.0 A) in Attached State

Table 4.1: OUT1 e OUT2 pin settings.

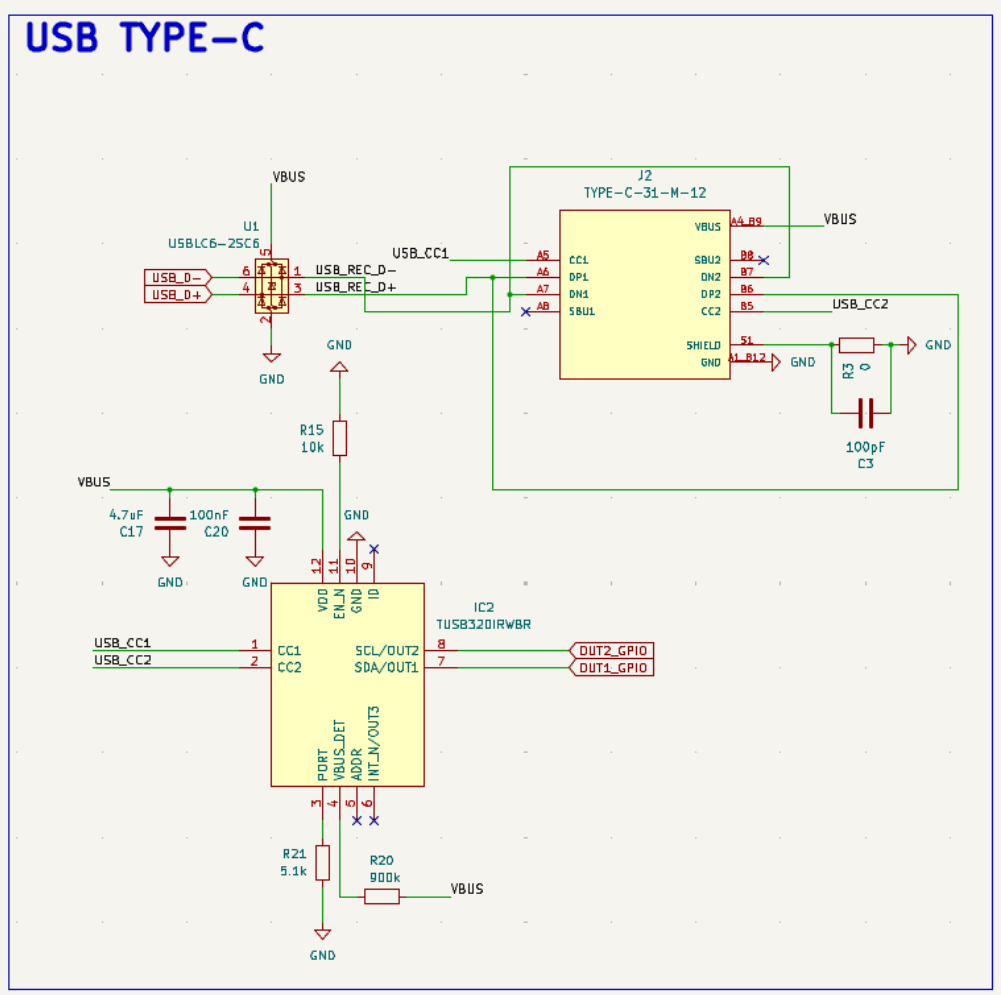

Figure 4.4: USB Type-C® design.

4.3 Power supply design

The power management design of this project(figure 4.5 and 4.8) is mainly divided into four sections:

- LDO (Low Dropout Regulator) for power conversion from 5 V to 3.3 V.
- Decoupling capacitors for the STM32 MCU power supply.
- Battery charging circuitry.
- Boost converter from 4.4 VV to 5 V.

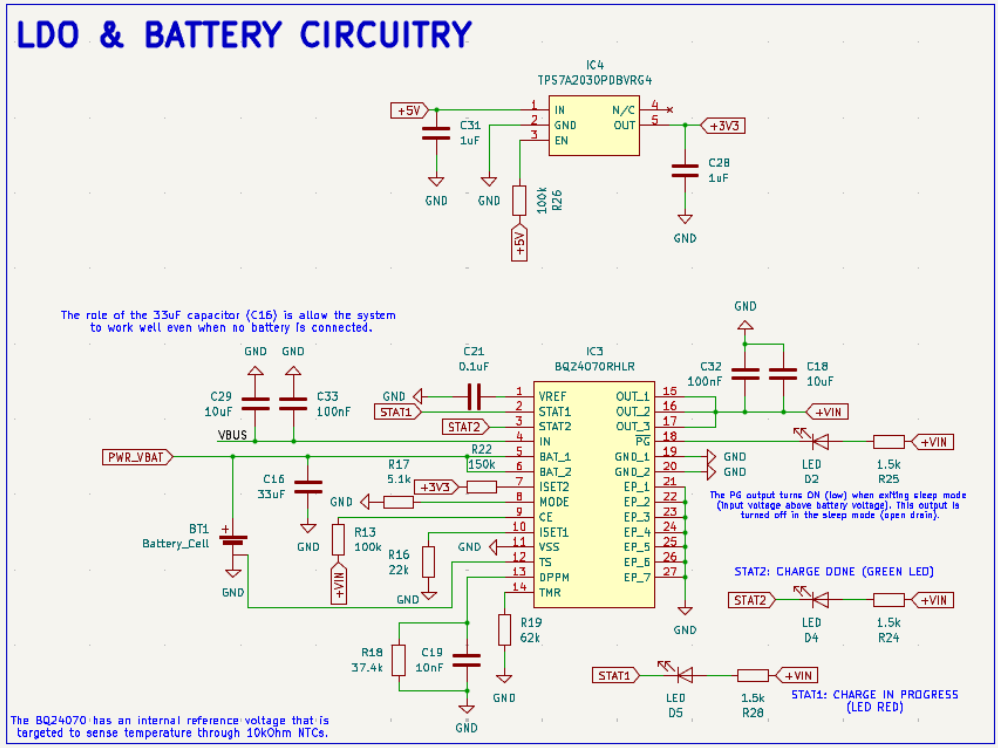

Figure 4.5: LDO and Battery charging circuitry.

4.3.1 Low Drop Output(LDO)

In DC/DC conversion, there are two primary methods: linear regulators and switching mode power supplies (SMPS)[18]. Linear regulators offer a low-cost and simple way to regulate voltage. They provide only step-down regulation with a small voltage drop, $V_{\text{out}} \leq V_{\text{in}} - V_{\text{dropmin}}$. Low Dropout Regulators (LDOs) are linear regulators with a low voltage drop, typically in the range of 100 mV to 500 mV, which allows the output voltage to remain very close to the input voltage. Compared to SMPS, LDOs introduce relatively little noise, making them preferred for low-noise applications. They are characterized by their intrinsic noise and Power Supply Rejection Ratio (PSRR). These regulators are usually fully integrated and require only a few simple external components, such as resistors or capacitors. To regulate the output voltage, an LDO dissipates the voltage difference as heat. The power dissipated is given by equation 4.1.

$$P_{\text{dissipated}} = (V_{\text{in}} - V_{\text{out}}) \cdot I_{\text{out}} \tag{4.1}$$

The main drawback of LDOs is their efficiency, which can be approximated as equation 4.2.

$$\alpha \simeq \frac{V_{\text{out}}}{V_{\text{in}}} \quad (\text{valid for } I_Q \ll I_{\text{out}}) \tag{4.2}$$

where I_Q is the quiescent current. Efficiency becomes particularly low when the difference between V_{in} and V_{out} is large.
For this project, the selected LDO (figure 4.4) is the TPS7A20 by Texas Instruments[19].
The TPS7A20 is an ultra-compact linear regulator capable of delivering up to 300 mA of output current. It is optimized for applications requiring very low noise, high PSRR(Power Supply Rejection Ratio), and strong transient response, making it suitable for RF and other sensitive analog circuits. Thanks to advanced design techniques, it achieves ultra-low noise performance without requiring an external noise bypass capacitor. The device operates with input voltages from 1.6 V to 6.0 V and provides adjustable outputs from 0.8 V to 5.5 V, offering flexibility across many use cases. It ensures high accuracy (up to 1.5%) over variations in load, line, and temperature through an internal precision reference. Additional features include internal soft-start to reduce inrush current at startup, stability with small ceramic capacitors for compact implementations, low quiescent current ideal for battery-powered systems, and a smart enable circuit with an internal pulldown resistor that prevents unintended activation when the EN pin is left floating. In this case, a high voltage ($> V_{\text{EN(HI)}}$) on this pin enables the regulator off by default.

4.3.2 Decoupling

To provide a stable voltage without variations or noise, decoupling is a key element in power supply design. Supply voltage fluctuations are caused by load (current) variations and by the power conversion stage (LDOs, SMPS, etc.).
Decoupling consists of placing energy storage elements at different nodes of the power supply network to locally supply transient currents. These energy storage elements are capacitors placed as close as possible to circuits that generate transients. The goal is to minimize the size of the current loops in order to reduce parasitic resistance and inductance. For this reason, these capacitors are placed as close as possible to each $V_{\text{DD}}/V_{\text{SS}}$ pair. In the figure 4.6, the V_{DD} pins are not located close to the V_{SS} pins; therefore, the capacitors have been placed close to the V_{DD} pins and connected directly to the ground plane.
Bulk capacitors are also important at this design stage. They provide energy to the system to prevent voltage drops, typically having large capacitance values and being placed near the power supply entry point.
In practice, the distinction between decoupling, bypass, and bulk capacitors is not strictly defined, as all are used to stabilize the supply voltage. Generally speaking, bulk capacitors have higher capacitance values and can supply larger currents for

longer durations, thus filtering lower-frequency variations.
Additionally, in power supply design, these capacitors play two other major roles:

- Filtering noise from the power supply itself, especially ripple from SMPS converters and noise coming from the main power source.
- Ensuring stability and proper operation of the power supply feedback regulation loops, which require appropriate output capacitance to maintain stability and accuracy.

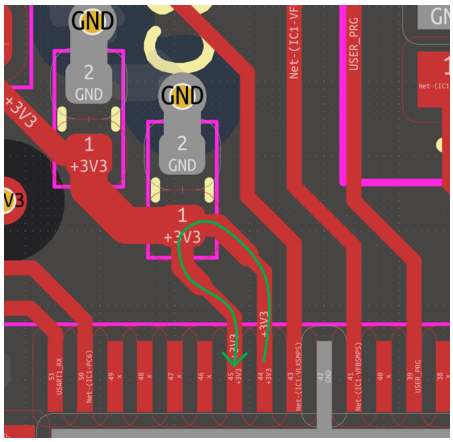

Figure 4.6: Short current loop.

4.3.3 Battery charging circuitry

An important feature implemented in the system is the battery charging circuit, designed to make the entire device portable. The idea is that when a charger is connected to the USB-C® port, the board is powered directly from the cable, while the onboard battery is simultaneously charged and bypassed. This functionality is provided by the BQ24070 from Texas Instruments[20], which enables power-path management(figure 4.7) between the external supply and the battery.

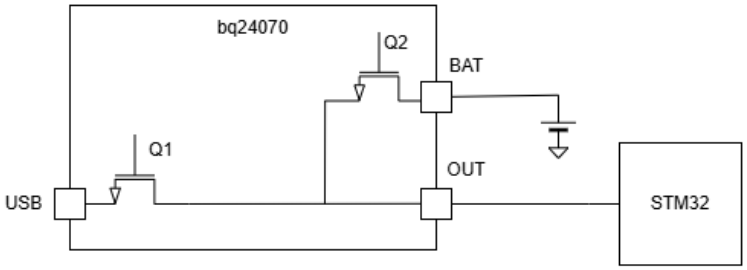

Figure 4.7: Power-Path Management.

The BQ24070 is a highly integrated Li-ion linear charger and system power-path management device, designed for space-constrained portable applications. It provides comprehensive DC supply (AC adapter) power-path management, including autonomous power-source selection, integrated power FETs and current sensors, precise current and voltage regulation, charge status monitoring, and charge termination, all within a single monolithic IC.
The BQ24070 can power the system while independently charging the battery. This capability reduces the number of charge and discharge cycles, ensures proper charge termination, and allows the system to operate even with a missing or faulty battery pack. It also enables the system to power on immediately from an external source, even if the battery is deeply discharged. The IC is specifically designed to maintain continuous system power, whether sourced from an AC adapter or the battery. In this case the system load is powered from a USB port (selecting MODE(PIN 8) = HIGH) through the internal transistor Q1(figure 4.7). This feature work as follow:

- **System Power**
  Q1 regulates the total input current to 500 mA, as configured through the ISET2 input. The output voltage (V_{OUT}) is regulated to 4.4 V. The system power management must ensure that the system load remains below the selected USB current limit, particularly when the battery is critically low or absent. If this condition is not met, the output voltage will drop to the battery voltage. For this reason, the system should implement a low-power operating mode when powered via USB. The Dynamic Power Path Management (DPPM) feature prevents the output voltage from falling below the programmed threshold during battery charging by automatically reducing the charging current.
- **Charge Control**
  The charge current to the battery is set by the ISET1 resistor. Because the programmed charging current is usually set higher than the maximum current allowed by the USB input, the output voltage can drop to either the battery voltage or the DPPM voltage, whichever is higher. If the DPPM threshold is reached first, the charging current is reduced until V_{OUT} stops decreasing. If V_{OUT} drops to the battery voltage, the battery can supply additional current to support the system load.
- **Dynamic Power-Path Management(DPPM)**
  This feature monitors the output voltage (system voltage) to detect input power loss caused by brownouts, current limiting, or removal of the input supply. If the voltage at the OUT pin drops to a preset level, $V(DPPM) \cdot SF$, due to limited input current, the battery charging current is reduced until the output voltage stops decreasing. The DPPM control attempts to establish a steady-state condition in which the system receives the required current and the battery is charged with the remaining available current. There is no active

control that limits the current delivered to the system; therefore, if the system demands more current than the input source can supply, the output voltage falls slightly below the battery voltage and Q2 turns on, allowing the battery to supplement the input current to the system.

Detailed design procedure

Figure 4.7 shows the schematic of the BQ24070, followed by the design steps that were implemented.

1. 100 nF capacitors are placed on IN and OUT. Additional 10 µF capacitors are included on IN and OUT to improve load transient response. The role of the 33 µF capacitor (C16) is to ensure proper hot-plug power up with a no-load condition (no system load or battery attached).
2. $$R_{\mathrm{SET1}}(R16) = \frac{V_{(\mathrm{SET})} \cdot k_{(\mathrm{SET})}}{I_{\mathrm{O(BAT)}}} = \frac{5\,\mathrm{V} \cdot 450}{100\,\mathrm{mA}} = 22.5\,\mathrm{k\Omega} \rightarrow 22\,\mathrm{k\Omega}$$

   The R_{SET} resistor, connected between the ISET1 and VSS pins, determines the charge level.
3. $$R_{\mathrm{SET2}}(R22) = 150\,\mathrm{k\Omega}$$

   This pull-up resistor is used to set the charge current to 500 mA for the USB port.
4. $$R_{\mathrm{TMR}}(R19) = \frac{t_{\mathrm{CHG}}}{K_{\mathrm{TMR}}} = \frac{6\,\mathrm{hr} \cdot 60\,\mathrm{min\,h^{-1}} \cdot 60\,\mathrm{s\,min^{-1}}}{0.360\,\mathrm{s\,\Omega^{-1}}} = 60\,\mathrm{k\Omega} \rightarrow 62\,\mathrm{k\Omega}$$

   This resistor determines the charge time in charge mode.
5. $$R_{\mathrm{DPPM}}(R18) = \frac{V_{(\mathrm{DPPM\text{-}REG})}}{I_{(\mathrm{DPPM})} \cdot SF} = \frac{4.26\,\mathrm{V}}{100\,\mathrm{\mu A} \cdot 1.15} = 37.044\,\mathrm{k\Omega} \rightarrow 37.4\,\mathrm{k\Omega}$$

   A capacitor $C_{\mathrm{DPPM}}(C19)$ of 10 nF was added to prevent the IC from falsely entering short-circuit protection during start-up.
6. STAT1 and STAT2 are the charge status output pins. A red LED with a 1.5 kΩ series resistor is connected to this pin. The LED turns on while battery charging is in progress. On the other hand, a green LED is connected to the STAT2 pin, which lights up when the battery charging is complete.
7. A red LED is connected to the PG pin. The $\overline{PG}$ output turns ON (low) when exiting sleep mode (input voltage above the battery voltage) and is turned OFF in sleep mode (open-drain).

4.3.4 Boost converter

Another important and widely used implementation is the TPS61032 boost converter from Texas Instruments[21]. The TPS61032 device provides a power supply solution for products powered either by a single-cell Li-Ion or Li-Polymer battery, or by two to three cells of alkaline, NiCd, or NiMH batteries. The converter generates a stable output voltage, which can be set either by an external resistor divider or fixed internally on the chip.
It offers highly efficient power conversion and can deliver output currents up to 1 A at 5 V from supply voltages as low as 1.8 V. The implemented boost converter uses a fixed-frequency pulse-width modulation (PWM) controller with a synchronous rectifier to achieve maximum efficiency. At low load currents, the converter enters *Power Save* mode to maintain high efficiency across a wide load range. This Power Save mode can be disabled, forcing the converter to operate at a fixed switching frequency, or it can be synchronized to an external clock signal applied to the SYNC pin.
The maximum peak current in the boost switch is limited to 4.5 A. The converter can be disabled to minimize battery drain; during shutdown, the load is completely disconnected from the battery. A low-EMI(Electromagnetic interference) mode is also included to reduce switching noise and radiated electromagnetic energy when the converter operates in discontinuous conduction mode.

Detailed design procedure

Figure 4.8 shows the schematic of the TPS61032, followed by the design steps that were implemented.

1. **Programming the output voltage**
   The output voltage of the TPS61032 DC/DC converter stage is adjustable through an external resistor divider network:

$$R42 = R41 \cdot (\frac{V_O}{V_{FB}} - 1) = 270\,\text{k}\Omega \cdot (\frac{5\,\text{V}}{500\,\text{mV}} - 1) = 2.43\,\text{M}\Omega \rightarrow 2.7\,\text{M}\Omega$$

   With $R42 = 2.7\,\text{M}\Omega \rightarrow R41 = 300\,\text{k}\Omega$
   This approximation introduces a relative error of 11.1% with respect to the ideal value.

2. **Programming the LBI/LBO threshold voltage**
   The low-battery detection circuit monitors the battery voltage and asserts an error flag when it falls below a user-defined threshold. The function is active only when the device is enabled; otherwise, the LBO pin is high-impedance. The LBI pin threshold is 500 mV.

During normal operation, LBO remains high-impedance while the LBI voltage is above the threshold and goes active low when it drops below 500 mV. The detection point can be programmed via a resistive divider at LBI, which scales the battery voltage to the 500 mV threshold for comparison.

$$R35 = R36 \cdot (\frac{V_{\text{BAT}}}{V_{LBI\text{- threshold}}} - 1) = 360\,\text{k}\Omega \cdot (\frac{4.4\,\text{V}}{500\,\text{mV}} - 1) = 3.04\,\text{M}\Omega \rightarrow 3.6\,\text{M}\Omega$$

With $R35 = 3.6\,\text{M}\Omega \rightarrow R36 = 470\,\text{k}\Omega \rightarrow V_{\text{BAT}} = 4.33\,\text{V}$
The calculated value of R_{35} is 3.04 MΩ. Since this value is not available in the standard resistor series, the closest commercial value 3.6 MΩ was selected. This approximation introduces a relative deviation of 18.4% in the resistor value. Consequently, the actual battery threshold voltage becomes 4.33 V instead of 4.4 V, corresponding to an error of approximately 1.6%.

3. **Inductor selection**
A boost converter generally relies on two key passive components to store energy during voltage conversion: the boost inductor and the output capacitor.

$$I_L = I_{\text{OUT}} \cdot \frac{V_{\text{OUT}}}{V_{\text{BAT}} \cdot 0.8\,\text{V}} = 1\,\text{A} \cdot \frac{5\,\text{V}}{4.33\,\text{V} \cdot 0.8\,\text{V}} = 1.44\,\text{A}$$

The maximum deliverable output current was fixed at 1 A. This value represents the system bottleneck, as it limits the maximum load current and therefore sets the required inductor current I_L.
The second parameter to consider when selecting the inductor is the desired current ripple. Typically, it is recommended to maintain a ripple of less than 20% of the average inductor current. A smaller ripple reduces magnetic hysteresis losses in the inductor, as well as output voltage ripple and EMI. However, it also increases the regulation time during load changes. Additionally, a larger inductor raises the overall system cost. Using these parameters, the inductor value can be calculated with:

$$L4 = \frac{V_{\text{BAT}} \cdot (V_{\text{OUT}} - V_{\text{BAT}})}{\Delta I_L \cdot f \cdot V_{\text{OUT}}} = \frac{2.9\,\text{V}}{(10\% \cdot I_L) \cdot 1\,\text{MHz} \cdot 5\,\text{V}} = 4\,\mu\text{H} \rightarrow 4.7\,\mu\text{H}$$

An inductor of 4.7 µH was selected from the standard component series. This represents a relative error of approximately 17.5% from the calculated value. The slightly higher inductance reduces the inductor current ripple, thereby improving the stability and performance of the converter.

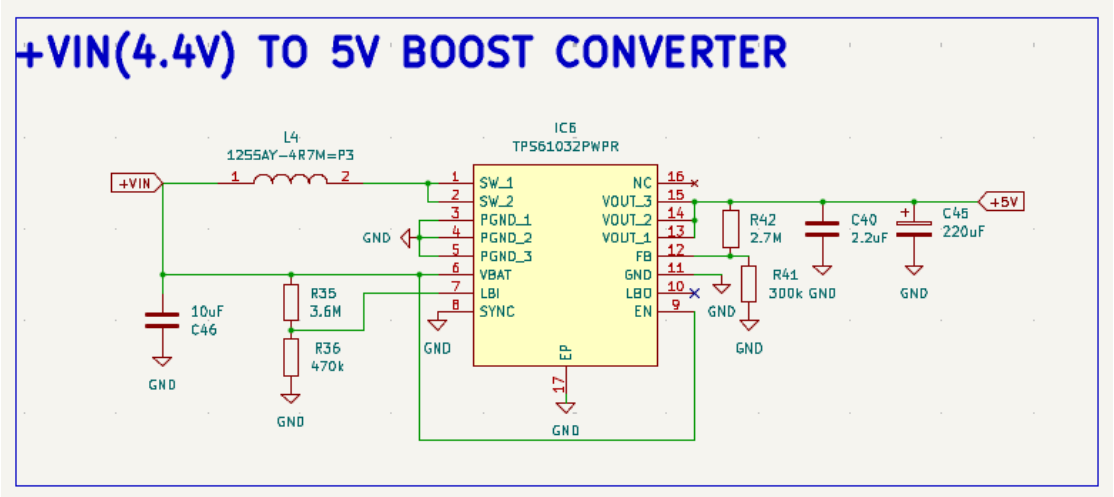

Figure 4.8: Boost converter.

4.4 Led Driver

4.4.1 Led Diode Driver-1

The voltage-controlled current source circuit shown in Figure 4.9 was used to drive a constant current into a signal or pump LED. This simple linear driver provides a constant stable current to the LED[22].
The basic circuit is a Howland current pump with a current booster (Q1) connected to the output of an R-R CMOS OPA350 operational amplifier (U1).

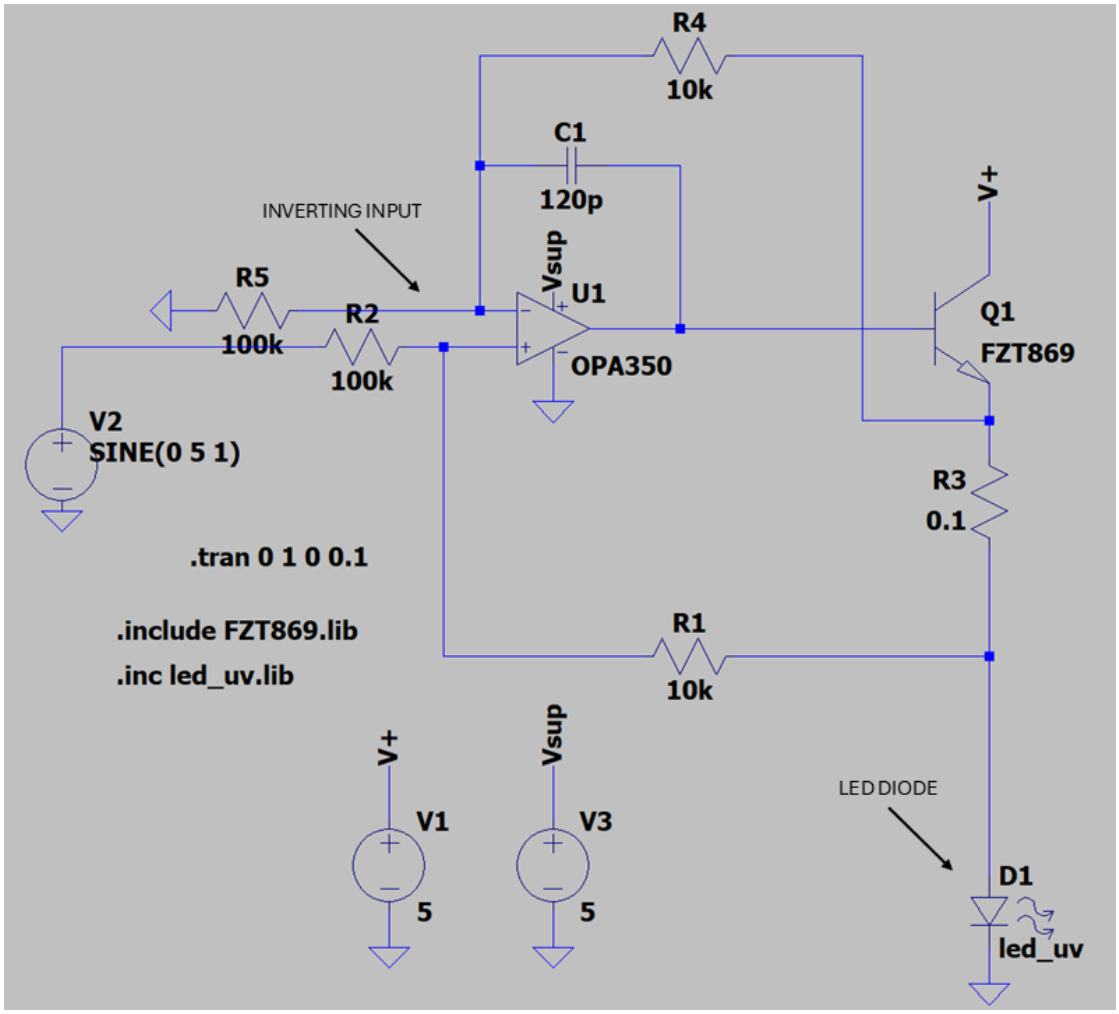

Figure 4.9: Led diode constant-current driver-1 circuit diagram.

The Howland current pump, invented in the early 1960s by Bradford Howland of Massachusetts Institute of Technology, consists of an operational amplifier and a balanced resistor bridge, and is capable of delivering current in either direction.

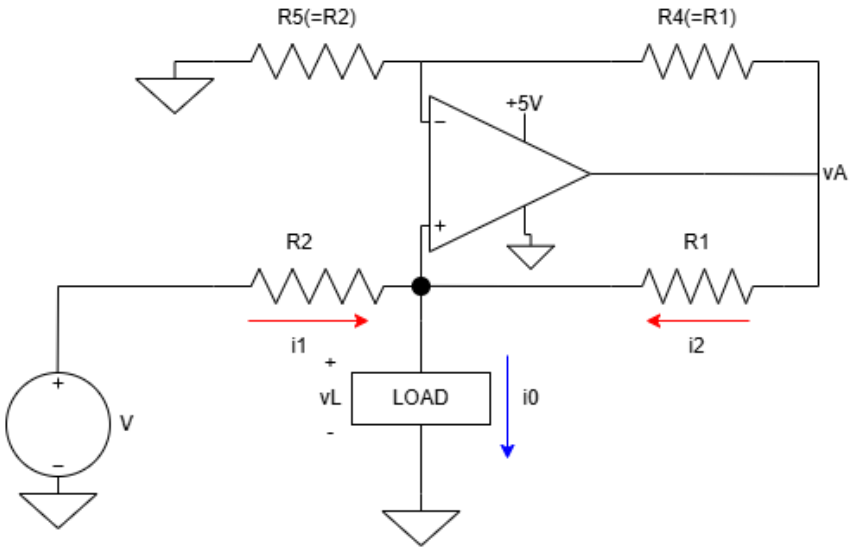

Figure 4.10: The Howland pump.

The Howland current pump, shown in figure 4.10, is a circuit that takes an input voltage v and converts it into an output current $i_O = Av$, where A is the transconductance gain. The circuit delivers the current i_O to a load L_D, independently of the load voltage v_L developed across it. To understand its operation, the labeling shown in figure 4.10 has been considered, and Kirchhoff's Current Law (KCL) together with Ohm's Law have been applied.

$$i_0 = i_1 + i_2 = \frac{v - v_L}{R_2} + \frac{v_A - v_L}{R_1} \tag{4.3}$$

The operational amplifier, together with R_5 and R_4, forms a non-inverting amplifier configuration with respect to (v_L), thereby yielding the corresponding amplified output.

$$v_A = (1 + \frac{R_4}{R_5}) \cdot v_L \tag{4.4}$$

Substituting v_A into Equation 4.3 and collecting, we put i_O into the insightful form

$$i_0 = Av - \frac{v_L}{R_o} \tag{4.5}$$

where A is the transconductance gain, in A/V,

$$A = \frac{1}{R_2} \tag{4.6}$$

and where R_o is the output resistance presented by the circuit to the load,

$$R_o = \frac{R_1}{\frac{R_1}{R_2} - \frac{R_4}{R_5}} \tag{4.7}$$

To ensure that i_O is independent of v_L, the output resistance R_O must approach infinity, that is, $R_O \to \infty$, which corresponds to satisfying the balanced-bridge condition.

$$\frac{R_4}{R_5} = \frac{R_1}{R_2} \tag{4.8}$$

If we set $R_1 = R_2 = R_4 = R_5 = 1\,\text{k}\Omega$ and $v = v_{\text{ref}} = 2\,\text{V}$. Consider the example shown in Table 4.2 and observe, row by row, how the operational amplifier adjusts i_2 through v_A to maintain the same output current i_O, regardless of the load voltage v_L.

$\boldsymbol{v_L(V)}$	$\boldsymbol{i_1(mA)}$	$\boldsymbol{v_A(V)}$	$\boldsymbol{i_2(mA)}$	$\boldsymbol{i_o(mA)}$
0	2	0	0	2
1	1	2	1	2
2	0	4	2	2
3	-1	6	3	2
-1	3	-2	-1	2
-2	4	-4	-2	2

Table 4.2: A 2 mA current source and its internal behavior for different values of v_L(a negative current indicates that the current flows in the direction opposite to the arrow).

With the polarity of V as shown in figure 4.10, the pump delivers i_O to the load. Reversing the polarity of V will cause the pump to draw i_O from the load. Note that for proper operation, v_A must remain within the linear range of the operational amplifier. If the op-amp enters saturation, the pump will no longer function correctly.
An analysis of the circuit shown in the figure 4.9 reveals the operation of the LED current driver, which is measured by sensing the voltage drop across a shunt resistor (R3) placed in series with the LED. The output current is controlled by the input voltage (V2), which can be provided either by an analog voltage source or by a voltage-output DAC.

In the configuration shown, the scale factor is 1 V at the input corresponding to 1 A at the output. The scale factor ($\frac{V_{IN}}{I_{OUT}}$) was set by choosing appropriate resistor values using the equation 4.9.

$$\frac{V_{IN}}{I_{OUT}} = \frac{R_2}{R_1} \cdot R_3 \; and, R_5 = R_2 = 100\,\text{k}\Omega, R_4 = R_1 = 10\,\text{k}\Omega, R_3(R_{SHUNT}) = 0.1\,\Omega \tag{4.9}$$

A LTspice simulation (sine(AC)) was performed on V2, varying the input voltage from 0 V to 5 V. The figure 4.11 shows the relationship between the LED diode current and the input voltage. The power dissipation of Q1 is also shown in figure 4.12. Operating on a supply voltage of 5 V, Q1 dissipates 3.8 W at an output current of 1 A. When operating with a 3.3 V power supply, Q1 dissipates approximately 1.5 W. This is well within the dissipation capabilities of the selected FZT transistor, since its SOT-223 package can effectively dissipate heat into the copper traces on the PCB.

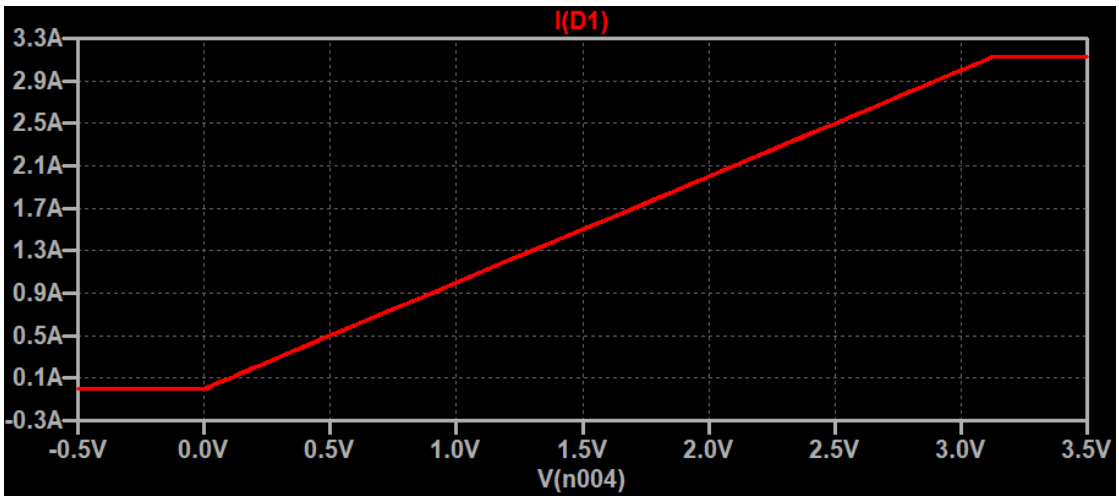

Figure 4.11: Output current versus input voltage with +5 V supply.

The LTspice probe output of a transient response simulation is shown in figure 4.13. The simulation uses a pulse source with amplitude varied automatically using the `.step` command. Four different pulse values are analyzed: 0.5 V, 1 V, 1.5 V, and 2 V, with the resulting curves overlaid on the same plot. The transient analysis covers a time interval long enough to observe the full pulse and the subsequent return of the output current to zero. The time resolution is sufficiently high to accurately capture the rising and falling edges. The circuit displays a clean response on both the rising and falling edges of the pulse, with no visible oscillations or instability. The power booster used for Q1 is a very high-gain single NPN transistor, not a Darlington device. It has a beta greater than 300 at a collector current of

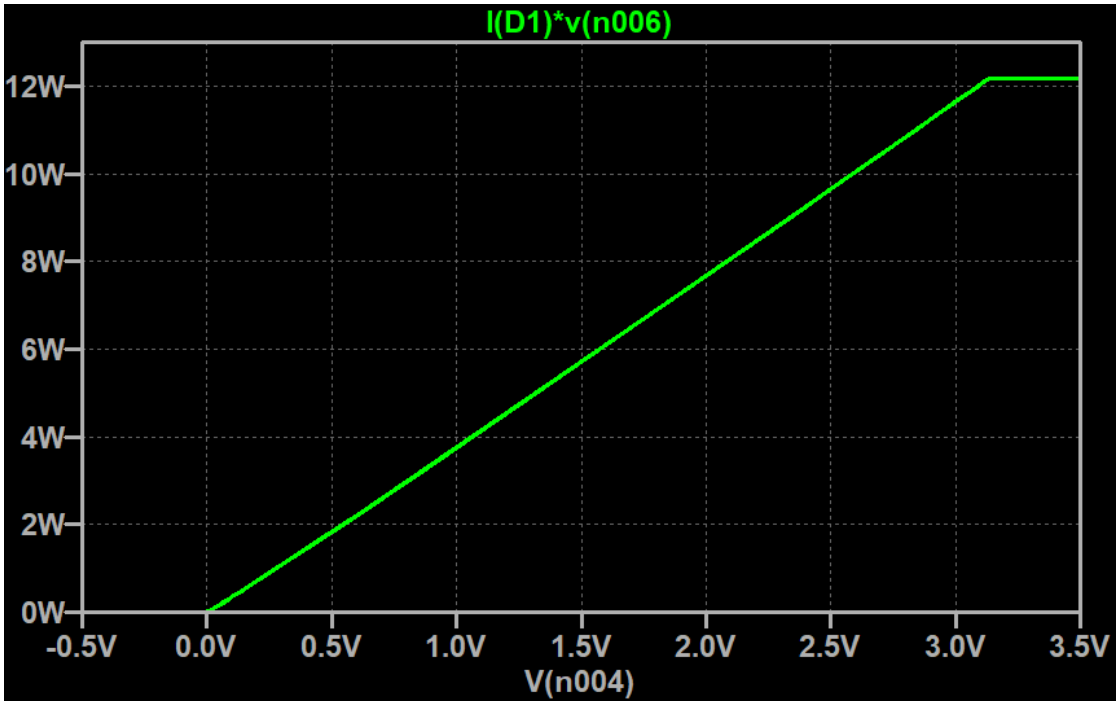

Figure 4.12: Q_1 power dissipation versus input voltage with +5 V supply.

1 A, which allows the CMOS OPA350 op-amp to drive it to high currents with ease. *Zetex* rates its continuous collector current at 6.5 A. However, the safe operating area (SOA) limits are reached well before this current is approached.

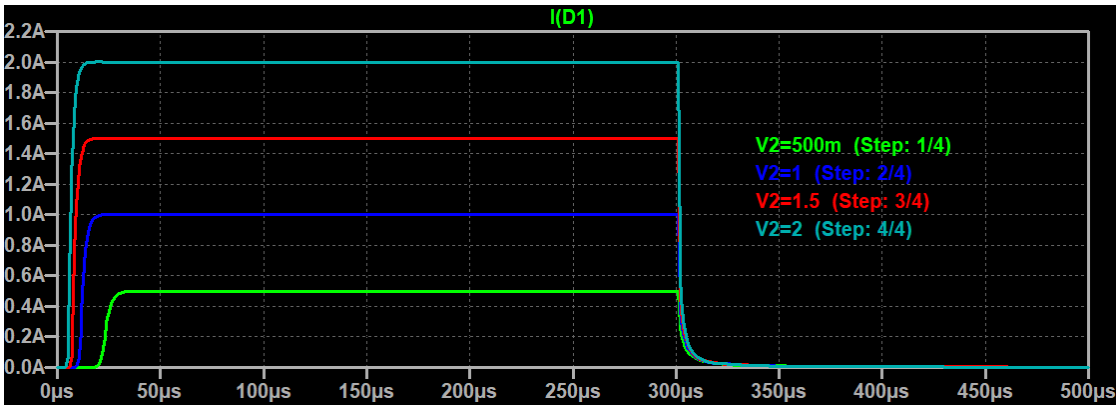

Figure 4.13: Led driver transient response with +5 V supply.

4.4.2 Led Diode Driver-2

Another circuit considered for implementing the LED driver is the voltage-controlled current source shown in Figure 4.14. This circuit can be used to deliver a very low-noise constant current to a signal or pump LED diode.
The basic configuration consists of an NPN transistor (Q1) acting as a current booster at the output of U2, a very low-noise bipolar operational amplifier, the OPA227. As illustrated, the scale factor is set so that an input voltage of -1 V corresponds to an output current of 1 A. The transfer ratio ($\frac{V_{\mathrm{IN}}}{I_{\mathrm{OUT}}}$) can be adjusted to different values by selecting appropriate resistor values according to the design equation 4.10.

$$\frac{V_{IN}}{I_{OUT}} = \frac{R_6}{R_1} \cdot R_2 \; and, R_6 = 10\,\mathrm{k}\Omega, R_1 = 1\,\mathrm{k}\Omega, R_2(R_{SHUNT}) = 0.1\,\Omega \tag{4.10}$$

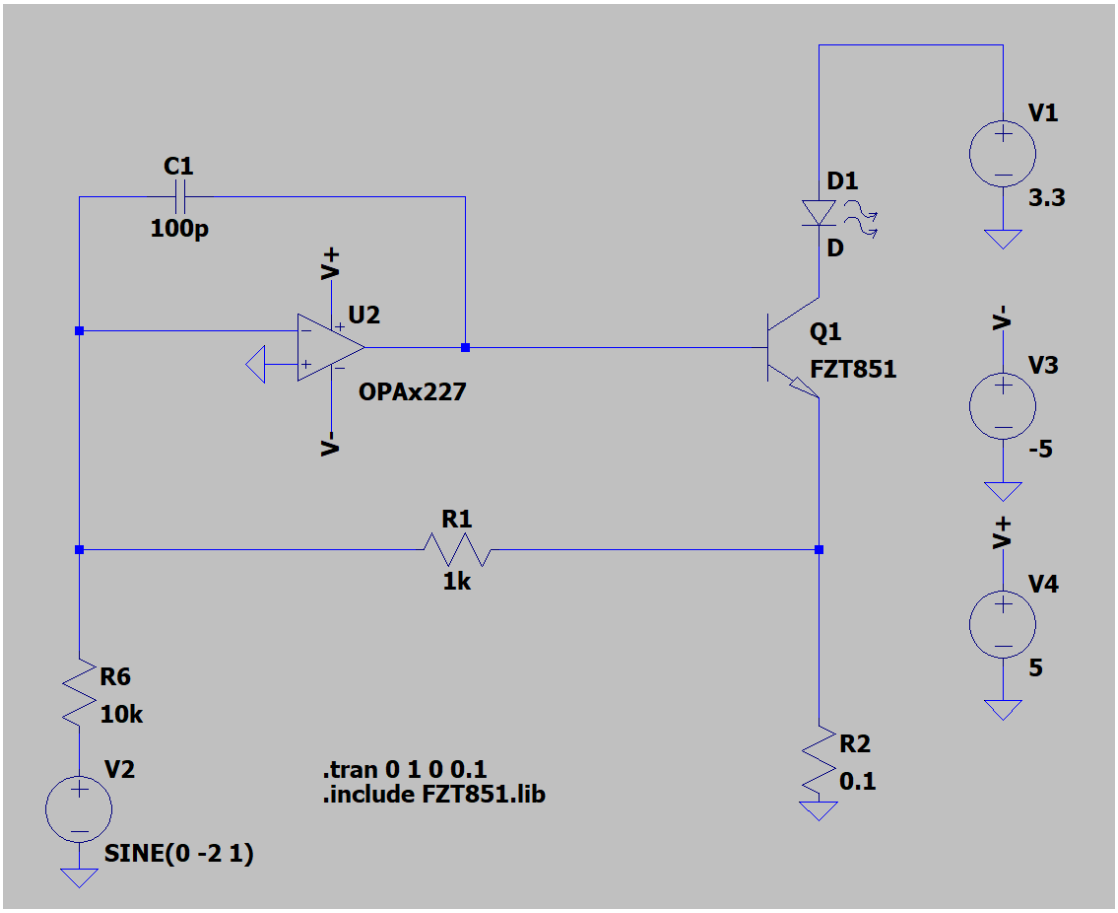

Figure 4.14: Led diode constant-current driver-2 circuit diagram.

A LTspice simulation (*sine(AC)*) was performed on V2, varying the input voltage from 0 V to -2 V. Figure 4.15 shows the relationship between the LED diode current and the input voltage. The power dissipation of Q1 is also shown in the figure 4.16. Q1 dissipates 2.5 W at an output current of 1 A.

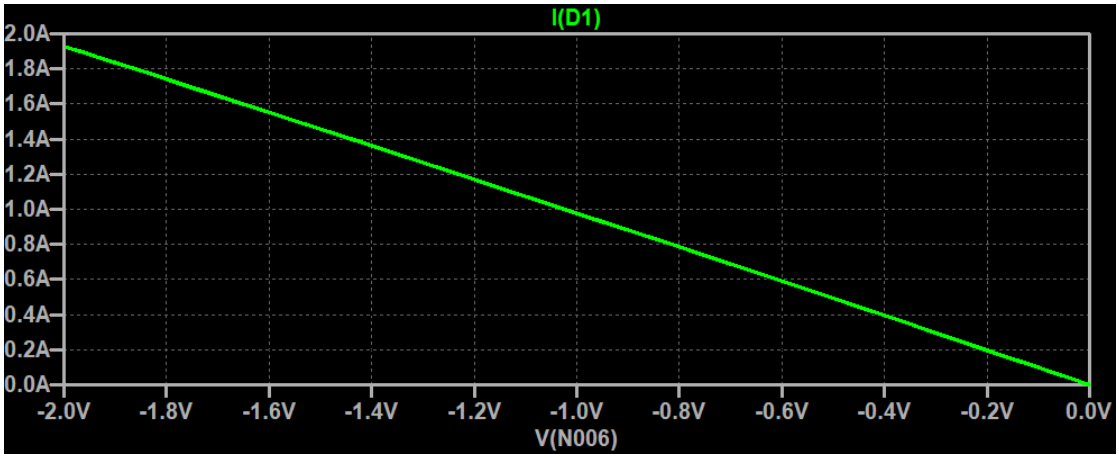

Figure 4.15: Output current versus input voltage with +3.3 V supply.

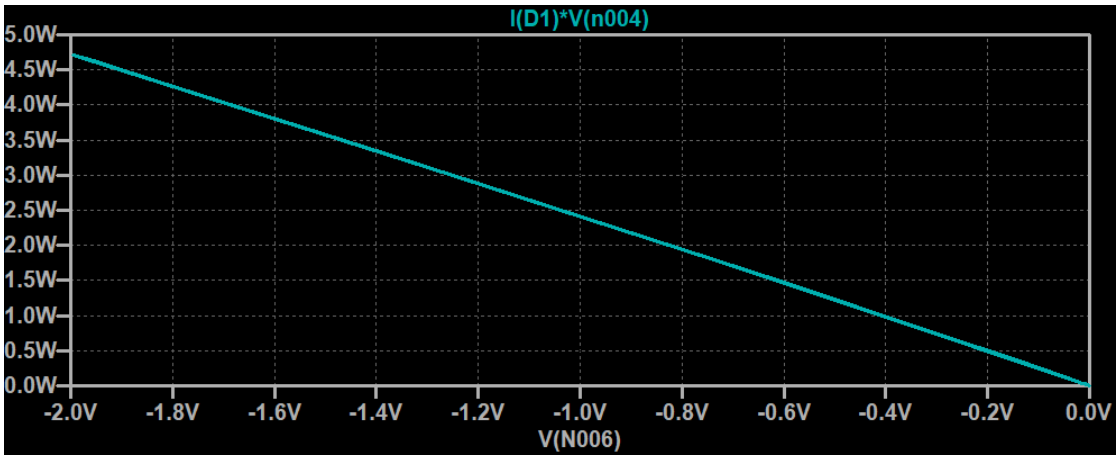

Figure 4.16: Q_1 power dissipation versus input voltage with +3.3 V supply.

The LTspice probe output for the transient response simulation is shown in figure 4.17. The simulation employs a pulse source whose amplitude is varied automatically using the `.step` command. Four different pulse amplitudes -0.5 V, -1 V, -1.5 V, and -2 V are analyzed, and the resulting waveforms are overlaid in a single plot.

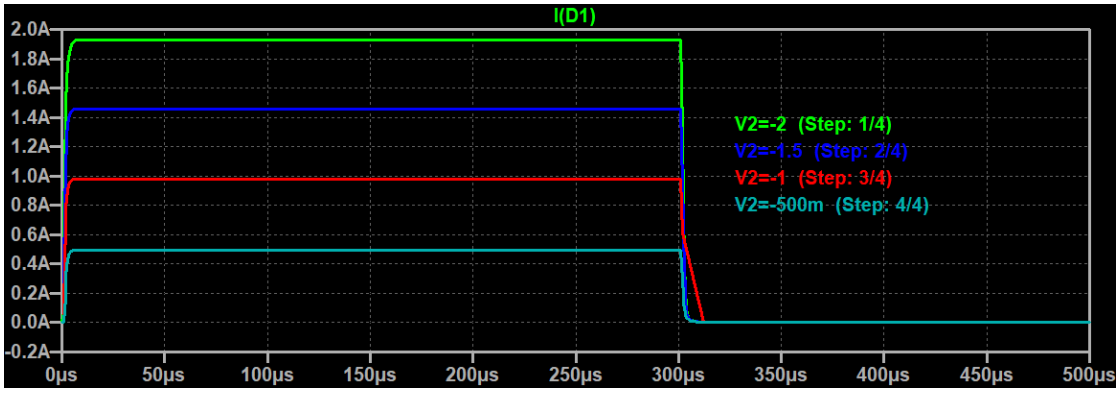

Figure 4.17: Led driver transient response with +3.3 V supply.

4.4.3 Switching circuit between PWM and Howland pump

For driving the LEDs used to illuminate the sample inside the cuvette, a switching circuit has been designed to select between two operating modes: PWM (Pulse Width Modulation) and a constant current source based on a Howland current pump, which level can be set through the MCU using a programmable DAC. PWM allows the control of light intensity by varying the duty cycle of a high-frequency switching signal (figure 4.18): the LED is rapidly turned on and off, and the average emitted intensity depends on the fraction of time it remains on. This approach provides high energy efficiency and straightforward intensity modulation, making it particularly suitable when adjustable illumination levels or synchronization with an acquisition system is required.

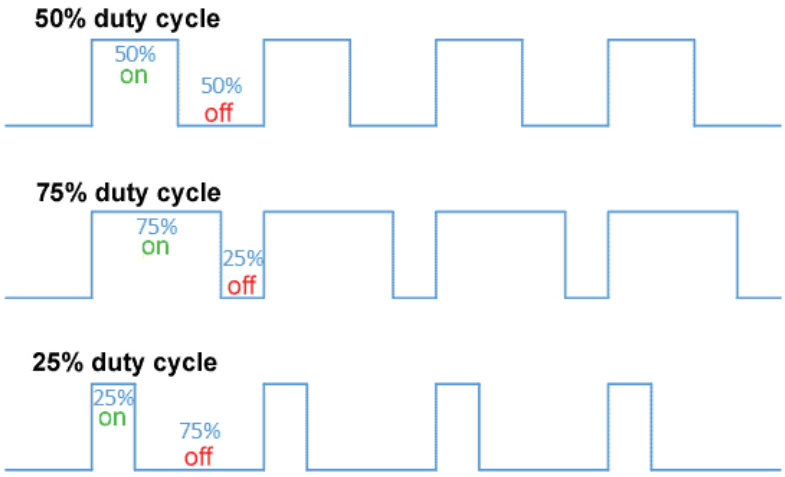

Figure 4.18: PWM duty cycle [23].

On the other hand, the Howland current pump provides an analog constant-current drive with high precision (the main bottleneck is the resolution of the input DAC for the voltage setpoint). Since the optical output of a LED is correlated to the current flowing through it, a stable current source ensures more consistent light emission. and reduces variations caused by temperature changes, supply fluctuations, or intrinsic LED nonlinearities[24]. This aspect is especially important in fluorescence measurements, where small fluctuations in excitation intensity can directly affect the emitted fluorescence signal from the beads.
The purpose of implementing both driving strategies is to experimentally investigate how the sample behaves under the two excitation conditions and to evaluate what differences may arise in the fluorescence response. Under PWM excitation, the fluorescence intensity is expected to follow the average optical power, although it may also depend on the modulation frequency relative to the excitation and decay dynamics of the fluorophores (in fact, PWM excitation involves brief, yet more intense bursts, which, when averaged over time, result in a lower overall intensity). Comparing these two approaches will make it possible to assess differences in fluorescence intensity, signal stability, signal-to-noise ratio, and the possible onset of effects such as saturation or photo-bleaching, thereby guiding the optimization of the excitation system for the sample.

The two LED drivers can switch between two types of supply (Howland and PWM). To do so a proper switching logic has been designed, so that it could reroute the desired kind of supply to the desired load.
In principle, this functionality could be implemented using simple analog switches. However, commercially available analog switches typically cannot support currents higher than about 300 mA. For this reason, an "analog fashion-like" circuit (figure 4.19) based on PMOS and NMOS transistors was designed. This solution overcomes the current limitations of commercial analog switches while remaining easy to implement and cost-effective.

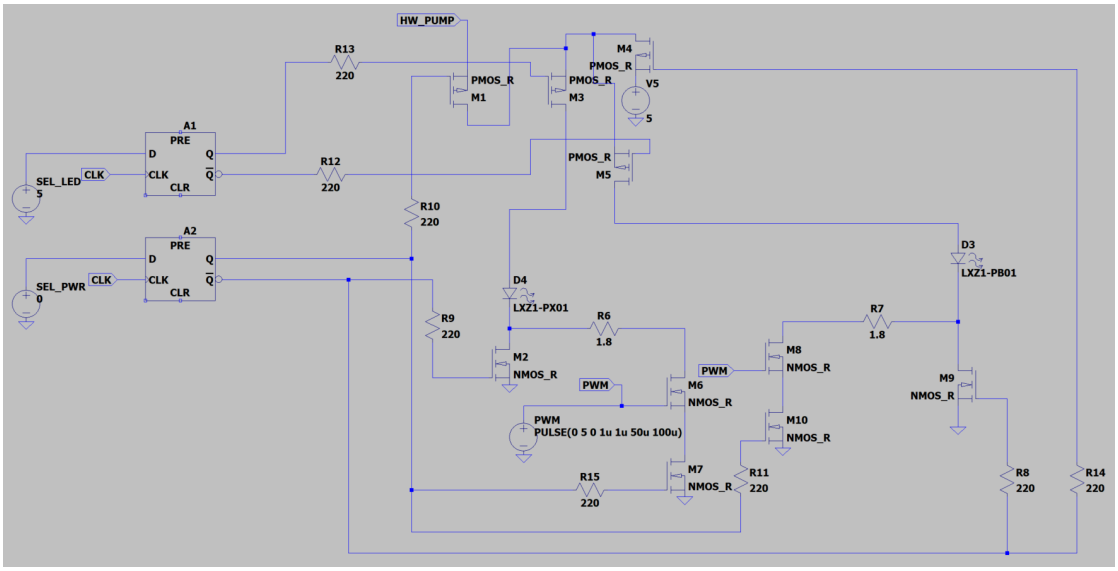

Figure 4.19: Schematic of the switching circuit for LED and power supply selection (Howland pump or PWM).

Let's now analyze the differences between NMOS and PMOS MOSFETs and their operation as switches. A high-side input switch can be implemented using either an N-channel or a P-channel MOSFET.

N-channel high-side MOSFET:

The switch disconnects the supply voltage when the gate voltage is low. To fully turn it on and connect the supply to the downstream circuit, the gate voltage must exceed the supply voltage by at least the MOSFET's threshold voltage. This requires additional circuitry, such as a charge pump, when using an N-channel MOSFET as a high-side input switch. Some protection circuits integrate a comparator and a charge pump to drive the N-channel high-side MOSFET, keeping the solution relatively simple.

P-channel high-side MOSFET:

Using a P-channel MOSFET as a high-side switch does not require a charge pump, but the control signal polarity is inverted. This approach is common in many applications due to its simplicity.

When a P-channel MOSFET is used, it is necessary to properly define the biasing of the gate, source, and drain terminals. The gate-source voltage (V_{GS}) plays a key role in controlling MOSFET conduction. For a P-channel MOSFET, the gate

voltage must be lower than the source voltage by at least the threshold voltage, ensuring that the MOSFET operates in its active region and allows current to flow from source to drain.
The gate-source threshold voltage ($V_{GS(th)}$) specifies the minimum voltage between gate and source required to form a conductive channel. For P-channel MOSFETs, $V_{GS(th)}$ is typically negative, indicating that the gate must be sufficiently negative relative to the source to allow conduction.
Finally, the drain-source voltage (V_{DS}), i.e., the voltage applied between drain and source, must be considered, ensuring that the device operates within the specified limits to prevent damage.
The solution shown in the figure 4.19 employs a PMOS for high-side switching and an NMOS for low-side switching. The PMOS turns on when the gate voltage is lower than the source voltage. Since the source is connected to V_{CC}, the PMOS can be easily driven by logic signals, making control straightforward and efficient. The MOSFETs used are the PMOS DMG3401LSN-7 (Diodes Incorporated)[25] and the NMOS SI2304DDS-T1-BE3 (Vishay/Siliconix)[26]. The specifications are shown in table 4.3.These devices were selected by estimating the maximum load current that will flow through the MOSFET and ensuring that the maximum drain voltage exceeds the highest V_{DD} level present in the circuit.
The gate threshold voltage ($V_{GS(th)}$) and the maximum gate-to-source voltage were also taken into account to ensure safe operation of the MOSFET. Another critical factor is the on-state drain-source resistance ($R_{DS(on)}$), which should be as low as possible to minimize power losses and improve circuit efficiency. Finally, the maximum power dissipation of the device was evaluated to ensure that the MOSFETs can operate without exceeding thermal limits.

Specifications	***PMOS***(DMG3401LSN)	***NMOS***(SI2304DDS)
V_{DS} (Drain-Source Breakdown Voltage)	30 V	30 V
I_d (Continuous Drain Current)	3.7 A	3.6 A
$R_{ds(on)}$ (Drain-Source Resistance)	50 mΩ	60 mΩ
$V_{gs(th)}$ (Gate-Source Threshold Voltage)	500 mV	1.2 V
P_d(Power Dissipation)	800 mW	1.7 W

Table 4.3: Specifications MOSFET.

Figure 4.19 shows that the source of the PMOS (M1) is connected to the Howland pump circuit. To enable the selection of one of the LED outputs and one of the two power supplies, two D-type flip-flops were used. Each flip-flop receives at its D input the corresponding control signal: SEL_LED (to select turning on LED D4 or D3) and SEL_PWR (to select the Howland or PWM power supply).
Based on these two control signals, the PMOS and NMOS transistors turn on or off, and all possible combinations of the control signals are listed in the table 4.4.

SEL_LED	***SEL_PWR***	***MOS(ON)***	***MOS(OFF)***
L(D4 ON)	L(HP)	M1,M2,M3	M4,M5,M6,M7,M8,M9,M10
L(D4 ON)	H(PWM)	M3,M4,M6,M7	M1,M2,M5,M8,M9,M10
H(D3 ON)	L(HP)	M1,M5,M9	M2,M3,M4,M6,M7,M8,M10
H(D3 ON)	H(PWM)	M4,M5,M8,M10	M1,M2,M3,M6,M7,M9

Table 4.4: Control signal combinations and transistor states.

Based on the type of LED selected, as described in the previous chapter, the four current-sense resistors connected in series with the LED were carefully sized. These components play a crucial role when the LED is driven by a PWM supply.
SMD thick-film resistors with an appropriate power rating were selected to ensure correct circuit operation and to prevent overheating during operation. The following section presents the dimensioning of these resistors, taking into account the forward current (I_{F}) and the forward voltage (V_{F}).

- **LED ULTRAVIOLET 365 nm**

$$R = \frac{V_{\mathrm{DD}} - V_{\mathrm{F}}}{I_{\mathrm{F}}} = \frac{5\,\mathrm{V} - 3.2\,\mathrm{V}}{0.8\,\mathrm{A}} = 1.25\,\Omega \rightarrow 1.2\,\Omega$$
$$P_{\mathrm{D}} = (0.8\,\mathrm{A})^2 \cdot 1.2\,\Omega = 0.768\,\mathrm{W}$$

- **LED ULTRAVIOLET 395 nm**

$$R = \frac{V_{\mathrm{DD}} - V_{\mathrm{F}}}{I_{\mathrm{F}}} = \frac{5\,\mathrm{V} - 3.4\,\mathrm{V}}{0.8\,\mathrm{A}} = 2\,\Omega \; P_{\mathrm{D}} = (0.8\,\mathrm{A})^2 \cdot 2\,\Omega = 1.28\,\mathrm{W}$$

- **LED BLU & GREEN**

$$R = \frac{V_{\mathrm{DD}} - V_{\mathrm{F}}}{I_{\mathrm{F}}} = \frac{5\,\mathrm{V} - 3.2\,\mathrm{V}}{1\,\mathrm{A}} = 1.8\,\Omega \; P_{\mathrm{D}} = (1\,\mathrm{A})^2 \cdot 1.8\,\Omega = 1.8\,\mathrm{W}$$

To implement two LED drivers, each supplying two LEDs, the circuit shown in the figure 4.19 was replicated for the second pair of LEDs. In order to obtain four D-type flip-flops, two dual-channel D-type flip-flops were implemented (figure 4.20). This configuration allows the management of three control signals:

1. *GPIO_SEL_OUT_*1 selects LED 1 and LED 2
2. *GPIO_SEL_OUT_*2 selects Howland pump or PWM
3. *GPIO_SEL_OUT_*3 selects LED 3 and LED 4

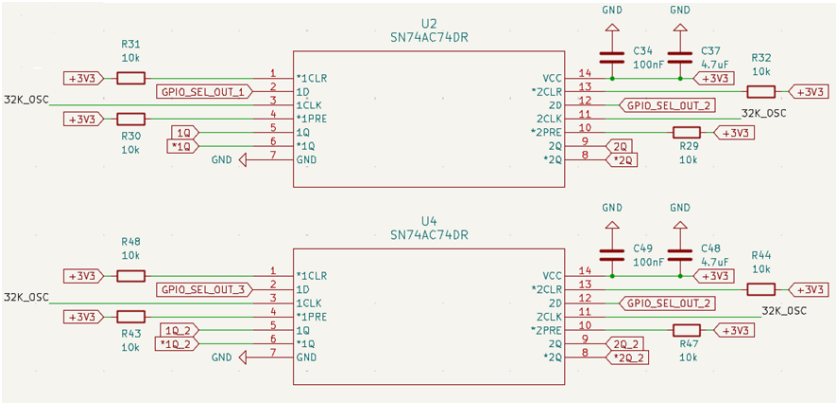

Figure 4.20: Two dual-channel D-type flip-flops.

In this section of the circuit, a dedicated 32 kHz oscillator was chosen to provide the clock signal, instead of sourcing it from the MCU. This solution ensures a stable and precise timing reference, independent of potential load variations or delays introduced by the MCU. Using an external oscillator also helps reduce jitter and signal interference, improving timing reliability and overall circuit synchronization. Additionally, the external oscillator is used for the logic of the safety circuit (explained in the following sections) and must operate independently from the MCU to guarantee reliable and autonomous safety functionality.

4.4.4 Schematic of the Howland current pump

As described in the previous section, two types of LED drivers based on the Howland current pump can be considered. For this project, LED diode driver-1 was selected because it can be easily implemented using a single 5 V power supply, which simplifies the overall circuit design and reduces both complexity and component count. This configuration allows straightforward integration with typical low-voltage electronic systems and avoids the need for additional power management stages.
In contrast, the second circuit topology operates with negative supply voltages. Implementing such a configuration would require additional components, such as a negative voltage generator or a dual power supply, increasing the hardware complexity, cost, and design effort. For these reasons, the first driver topology

represents a more practical and efficient solution for this application.
To generate the input voltage (V_{in}) required by the Howland current pump, a digital-to-analog converter (DAC) was employed. The use of a DAC allows a digital control signal generated by the control system to be converted into a precise and programmable analog voltage, enabling accurate regulation of the current delivered to the LED through the driver circuit.
For this purpose, the DAC7562SDGST (figure 4.21) from Texas Instruments was selected[27]. The DAC7562 is a low-power, voltage-output digital-to-analog converter featuring two channels and available with 16, 14, and 12 bit resolution. The device integrates a 2.5 V internal voltage reference with a temperature drift of 4 ppm $°C^{-1}$, enabling a full-scale output voltage range of 2.5 V or 5 V. The internal reference exhibits an initial accuracy of ±5 mV and is capable of sourcing or sinking up to 20 mA through the $V_{\text{REFIN}}/V_{\text{REFOUT}}$ pin.

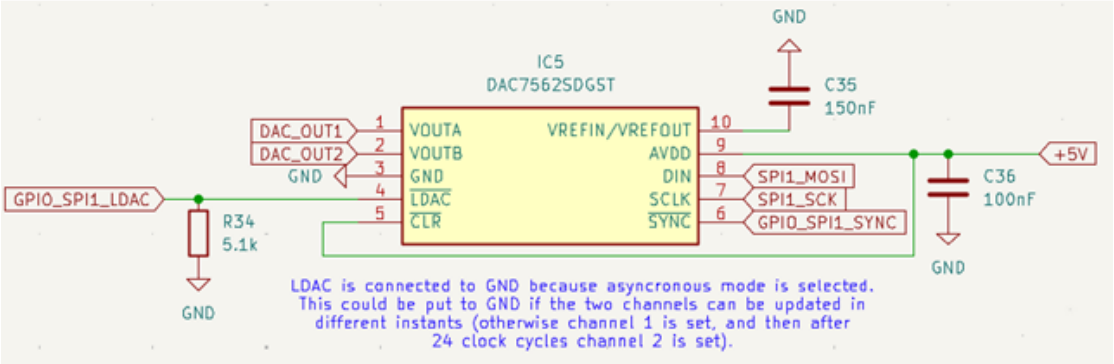

Figure 4.21: Digital-to-analog converter.

The DIN, $\overline{SCLK}$, and $\overline{SYNC}$ pins are connected to the microcontroller unit (MCU), enabling digital communication between the MCU and the DAC. The $\overline{LDAC}$ pin is connected to GPIO_SPI1_LDAC of the MCU, thereby selecting the asynchronous update mode. In this configuration, the two output channels can be updated independently at different time instants. Alternatively, if synchronous updating is required, the channels would be updated sequentially, with channel 1 being set first and channel 2 being updated after an additional 24 clock cycles.

The startup behavior of the Howland current pump was analyzed in detail to enable precise switching of the driver according to operational requirements. Since the OPA350 did not feature an enable pin, it was replaced with the OPA355NA_3K (figure 4.22), which provides this functionality. The output DRV_OUT_1 is connected to the switching circuit illustrated in the figure 4.19.

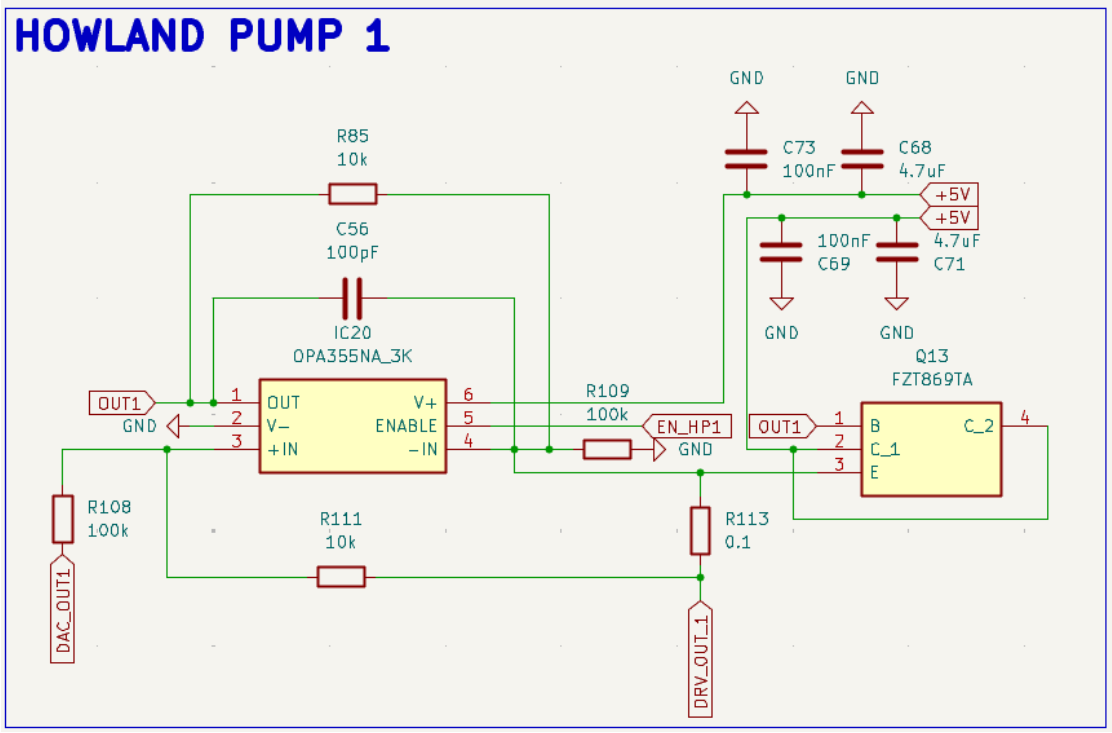

Figure 4.22: Howland pump with enable pin.

4.4.5 Security Circuitry

When the LED is powered on, it is considered good practice to analyze which components are activated and the effects that may occur when switching between LEDs or changing the power supply between HP and PWM modes. In particular, it is noted that the activation of the Howland pump requires that the MOSFETs in the switching circuit are enabled; without a load, the pump could immediately enter saturation, causing an undesirable current spike. Therefore, it is advisable to introduce a delay in the activation of the Howland pump to ensure a correct LED startup sequence.

The design approach aims to ensure that, upon changes in the logic signals GPIO_SEL_OUT_1 and GPIO_SEL_OUT_2, there is a delay such that the Howland pump is activated first (via the EN_HP_1 pin) and the MOSFETs in the switching circuit are enabled subsequently. This logic can be implemented either through software or via a dedicated hardware circuit. The hardware solution was selected because it provides a more stable and reliable LED activation, independent of potential microcontroller firmware errors.

Figure 4.23 shown that the input signals GPIO_SEL_OUT_1 and GPIO_SEL_OUT_2 are first processed through D and JK flip-flops, which stabilize

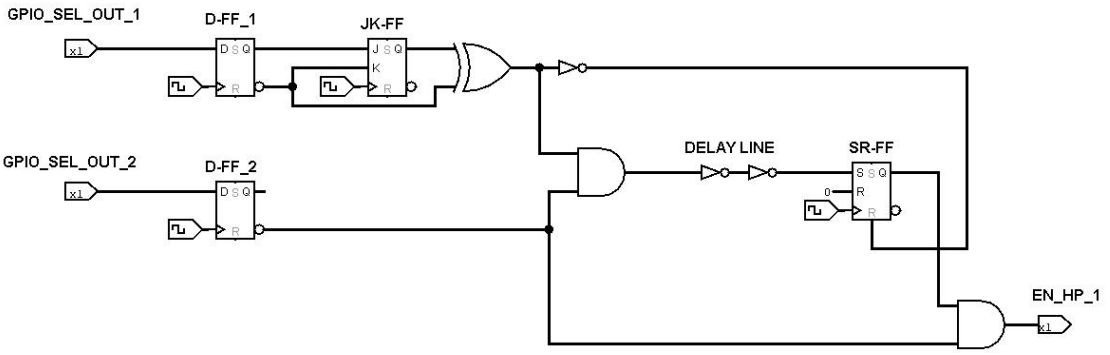

Figure 4.23: Security Circuitry.

the logic signals and introduce a controlled delay.
The outputs of the flip-flops are then combined using AND and OR gates, along with a delay line, to generate the final logic signal directed to the EN_HP_1 pin, which controls the activation of the Howland pump. This ensures that the Howland pump is enabled before the MOSFETs in the switching circuit, allowing a gradual and safe LED startup sequence.
The timing diagram of the safety circuit is shown in the figure 4.24. When GPIO_SEL_OUT_2 transitions from logic 0 to 1 (switching from the Howland Pump to PWM), EN_HP_1 is immediately driven low, disabling the Howland Pump until GPIO_SEL_OUT_2 returns to 0, at which point the pump is re-enabled. When GPIO_SEL_OUT_1 transitions from 0 to 1 (switching between two LEDs), EN_HP_1 is disabled after a two-clock-cycle delay. This ensures the Howland Pump is turned off, the current path is established, and EN_HP_1 is subsequently re-asserted.

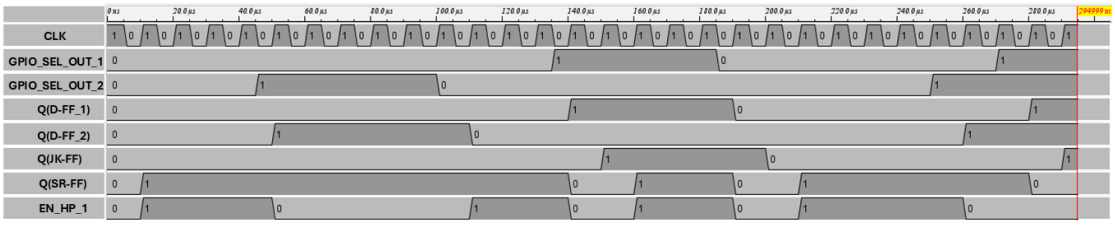

Figure 4.24: Timing diagram of security circuit.

After that it was analyzed the path consisting of a D flip-flop (SN74AC74DR) driving the J input of a JK flip-flop (HEF4027BT,653), both clocked by the same signal. The primary concern was whether the JK output would reflect the previous D value or the updated value in the same clock cycle. Clock path lengths were provided: 35.1 mm for the D and 92 mm for the JK, yielding a

differential of approximately 56.9 mm. Considering signal propagation in FR4 PCBs ($\sim$15 cm ns^{-1}), this corresponds to a clock skew of roughly 0.38 ns.
Typical datasheet parameters were analyzed:

- SN74AC74DR (D flip-flop, AC family): clock-to-Q propagation delay $\simeq$ 6 ns, setup time $\simeq$ 3–4 ns, hold time $\simeq$ 0.5–1 ns.
- HEF4027BT (JK flip-flop, CMOS 4000 series): setup time $\simeq$ 25–50 ns, clock-to-Q propagation delay $\simeq$ 30 ns.

The timing analysis demonstrates that the D output does not arrive at the JK's J input in time to satisfy the JK setup requirement. Consequently, the JK flip-flop captures the previous D cycle value, not the newly updated one. Potential conditions under which the JK might erroneously latch the new D value within the same clock cycle were also considered, identifying three critical factors: extremely fast D propagation, significant JK clock delay relative to D, or unrealistic environmental conditions (e.g., extreme voltage or temperature). Given the specified components and layout, these scenarios are not realized.

4.5 Temperature Sensing

The circuit illustrated in Figure 4.25 converts the analog voltage produced by an NTC thermistor, proportional to temperature, into a digital signal suitable for processing by the microcontroller.

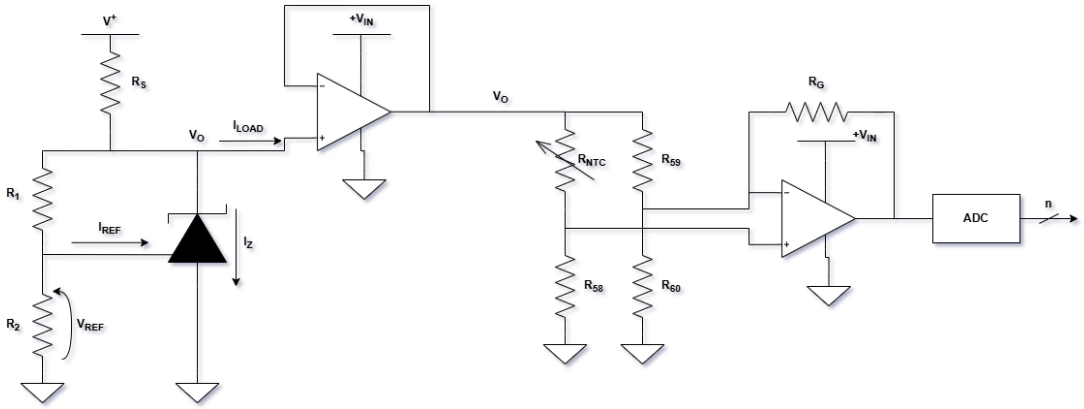

Figure 4.25: Temperature sensing circuit.

In the first stage of the circuit, a Zener diode configuration is implemented. In this case, the LM431 device has been employed. The LM431 is a three-terminal adjustable shunt regulator designed to ensure temperature stability across the full operating range while maintaining a stable reference voltage despite variations in the supply voltage. The output reference voltage is set to 2.5 V (V_{REF}) by selecting two external resistors that form a voltage divider network. The sizing of resistors R_S, R_1, and R_2 is presented below.

$$R_{\text{S-MIN}} = \frac{V_{+\text{-MAX}} - V_O}{I_{\text{LOAD-MIN}} + I_{\text{Z-MAX}}} = \frac{5\,\text{V} - 3.3\,\text{V}}{0 + 100\,\text{mA}} = 17\,\Omega \tag{4.11}$$

$$R_{\text{S-MAX}} = \frac{V_{+\text{-MIN}} - V_O}{I_{\text{LOAD-MAX}} + I_{\text{Z-MIN}}} = \frac{4.9\,\text{V} - 3.3\,\text{V}}{0 + 1\,\text{mA}} = 1.6\,\text{k}\Omega \tag{4.12}$$

Based on these two equations (4.11 and 4.12), the value of R_S was chosen as 1 kΩ. With equation 4.13 was calculated $R_1 = 15\,\text{k}\Omega$ and $R_2 = 47\,\text{k}\Omega$ with $V_{\text{REF}} = 2.5\,\text{V}$ and $V_O = 3.3\,\text{V}$.

$$V_{\text{O}} = (1 + \frac{R_1}{R_2}) \cdot V_{\text{REF}} \tag{4.13}$$

To achieve accurate temperature measurement, a Wheatstone bridge configuration was implemented, as shown in Figure 4.25. This topology enables precise detection of small resistance variations produced by the temperature sensor. The circuit also

incorporates amplification and filtering stages to enhance signal quality and reduce the effect of additive noise. Differential signal acquisition is adopted, allowing the instrumentation amplifier to effectively suppress common-mode disturbances. As a result, reliable measurements can be obtained even in electrically noisy environments.

$$V_{\mathrm{AB}} = V_A - V_B = V_O \cdot \left(\frac{R_{58}}{R_{58} + R_{\mathrm{NTC}}} - \frac{R_{59}}{R_{59} + R_{60}}\right) \tag{4.14}$$

Based on the equation 4.14, three values of V_{AB} were calculated at 25 °C,0 °C, and 50 °C, as shown below. In the Wheatstone bridge configuration, the resistors were selected as $R_{58} = R_{59} = R_{60} = 10\,\mathrm{k\Omega}$, using low-tolerance resistors in order to improve the measurement accuracy. The resistance R_{NTC} represents the resistance of the NTC temperature sensor. Although the sensor used in the circuit is an NTC thermistor, the resistance values at the considered temperatures were derived from a PT100 reference table for comparison purposes.

$$R_{\mathrm{NTC}} = 32.74\,\mathrm{k\Omega}\ @\ 0\,^{\circ}\mathrm{C} \rightarrow V_{\mathrm{AB}} = -0.8778\,\mathrm{V} \tag{4.15}$$

$$R_{\mathrm{NTC}} = 10\,\mathrm{k\Omega}\ @\ 25\,^{\circ}\mathrm{C} \rightarrow V_{\mathrm{AB}} = 0\,\mathrm{V} \tag{4.16}$$

$$R_{\mathrm{NTC}} = 3.604\mathrm{k\Omega}\ @\ 50\,^{\circ}\mathrm{C} \rightarrow V_{\mathrm{AB}} = 0.7757\,\mathrm{V} \tag{4.17}$$

Taking into account the gain of the instrumentation amplifier(INA3171):

$$G = 1.05 \rightarrow G = 1 + \frac{100\,\mathrm{k\Omega}}{R_g} \rightarrow R_g = 2\,\mathrm{M\Omega} \tag{4.18}$$

As the ADC accepts only positive input voltages, a precise reference voltage is required. This reference, $V_{\mathrm{REF+}}$, is provided by the STM32 microcontroller and is set to 2.048 V.

$$V = (V_{\mathrm{AB}} + V_{\mathrm{REF}}) \cdot G = 1.228\,\mathrm{V} \rightarrow\ @\ 0\,^{\circ}\mathrm{C} \tag{4.19}$$

$$V = (V_{\mathrm{AB}} + V_{\mathrm{REF}}) \cdot G = 2.1504\,\mathrm{V} \rightarrow\ @\ 25\,^{\circ}\mathrm{C} \tag{4.20}$$

$$V = (V_{\mathrm{AB}} + V_{\mathrm{REF}}) \cdot G = 2.9648\,\mathrm{V} \rightarrow\ @\ 50\,^{\circ}\mathrm{C} \tag{4.21}$$

The temperature resolution between 0 °C and 50 °C (equation 4.22) was determined based on the corresponding voltage range of the sensor and the resolution of the microcontroller's ADC.

$$\begin{aligned}
&\Delta V_{\text{sensor}} = V_{50\,^\circ\text{C}} - V_{0\,^\circ\text{C}} = 2.9648\,\text{V} - 1.228\,\text{V} = 1.7368\,\text{V} \\
&\text{Sensitivity: } \frac{\Delta V_{\text{sensor}}}{\Delta T} = \frac{1.736{,}8\,\text{V}}{50\,^\circ\text{C}} \approx 0.034736\,\text{V}\,^\circ\text{C}^{-1} \\
&\text{ADC resolution: } \Delta V_{\text{ADC}} = \frac{V_{\text{ref}}}{2^{12}-1} = \frac{2.048\,\text{V}}{4095} \approx 0.0005\,\text{V} \\
&\text{Temperature resolution: } \Delta T = \frac{\Delta V_{\text{ADC}}}{\text{V}\,^\circ\text{C}^{-1}} = \frac{0.0005\,\text{V}}{0.034736\,\text{V}\,^\circ\text{C}^{-1}} \approx 0.0144\,^\circ\text{C/step}
\end{aligned} \tag{4.22}$$

The calculation shows that, for the temperature range of 0–50 °C, the microcontroller's ADC can distinguish temperature changes as small as approximately 0.0144 °C per step, indicating very high measurement resolution within this range. The figure 4.26 shows the schematic of the temperature acquisition circuit. The circuit incorporates an analog switch, which allows it to be enabled or disabled via a control signal, EN_NTC. This approach optimizes power consumption, as the measurement circuit is powered only when temperature acquisition is required.

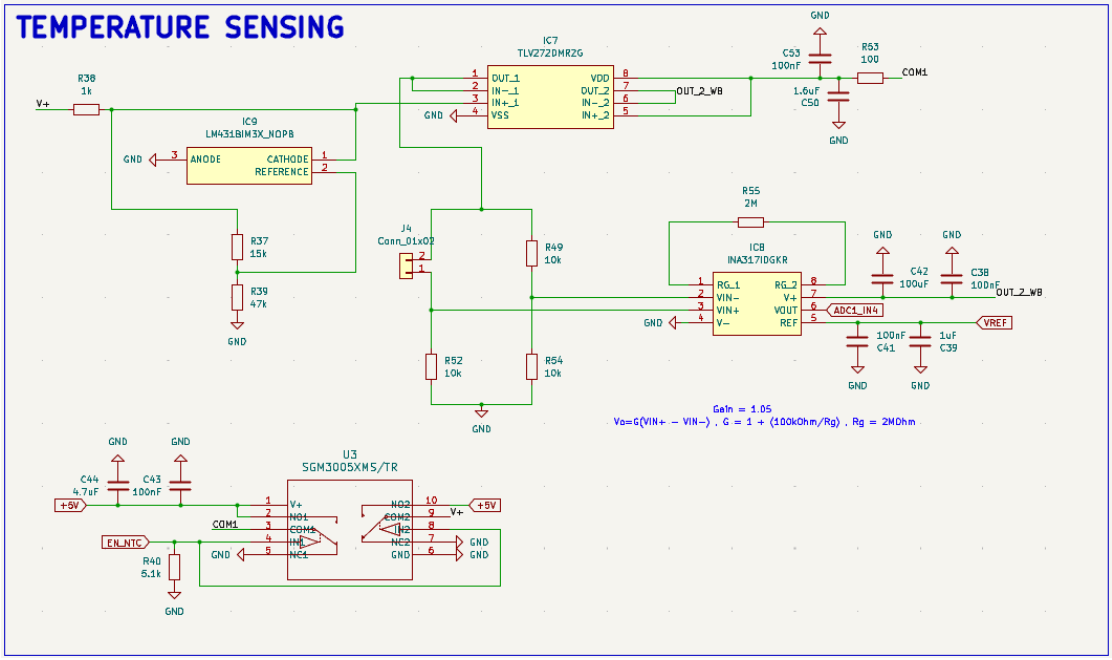

Figure 4.26: Temperature acquisition circuit.

4.6 Compact spectrometer data acquisition

For this project, a mini spectrometer manufactured by Adafruit was selected. The AMS AS7341 is an 11-channel spectrometer (figure 4.27) designed to enable new consumer, commercial, and laboratory applications. These include spectral identification, reflection and absorption analysis for color matching, fluid or reagent analysis, passive ambient light measurement, and color calibration.
The spectral response of the device is defined by individual channels covering approximately the 350 nm to 1000 nm wavelength range. Specifically, eight channels are centered in the visible spectrum (VIS), complemented by one near-infrared (NIR) channel and one clear channel. The NIR channel, in combination with the VIS channels, can provide information about surrounding ambient lighting conditions, including light source identification.
Light source detection is further supported by an integrated flicker detection channel, which can automatically detect ambient light flicker at 50/60 Hz and buffer data for the external calculation of other flicker frequencies up to 2 kHz.
The AS7341 integrates high-precision optical filters directly onto standard CMOS silicon through nano-optic deposited interference filter technology. Additionally, a built-in aperture regulates the amount of light entering the sensor array, thereby improving measurement accuracy.
The device also includes a programmable digital GPIO and an LED current controller, enabling control of the light source and trigger signals, as well as system expandability through the addition of an external photodiode. Device control and access to spectral data are implemented through a serial I²C interface.
Finally, the sensor is available in an ultra-low-profile package with dimensions of 3.1 mm × 2 mm × 1 mm, making it particularly suitable for integration into compact systems.
The benefits of AS7341, 11-Channel Multi-Spectral Digital Sensor, are listed below:

- Precision color, spectral composition and distribution measurements
- Low power consumption and efficient I²C communication
- Integrated ambient light flicker detection on chip and light source detection through NIR channel
- Electronic shutter/trigger and sync control
- External photodiodes to expand detection range

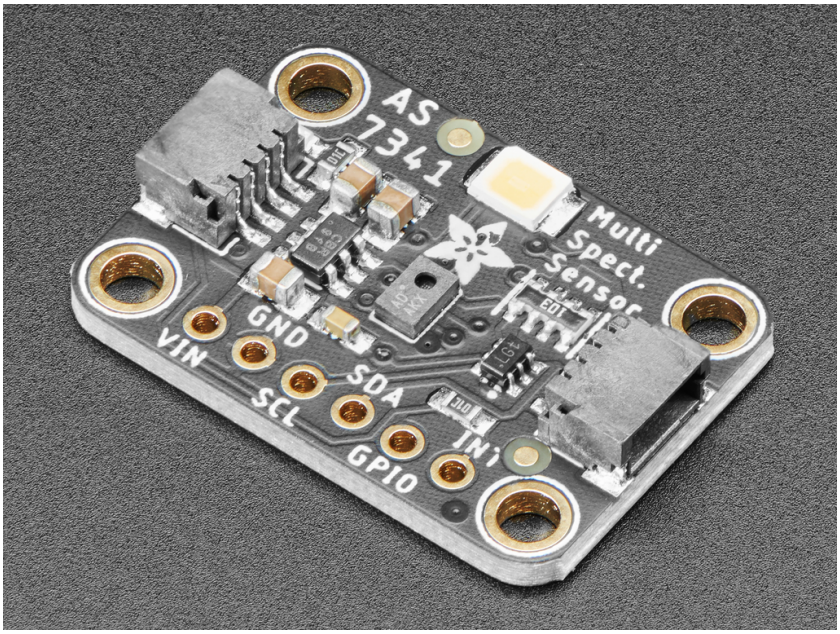

Figure 4.27: Adafruit AS7341 10-Channel Light[10].

The choice of this multispectral sensor is primarily motivated by the need for a compact and cost-effective device, enabling the development of a portable system capable of qualitatively monitoring the two types of beads and measuring their fluorescence intensity.
Table 4.5 summarizes the key optical properties of the device.

Channel	**Center Wavelength[nm] typical**	**FWHM[nm] typical**
F1	415	26
F2	445	30
F3	480	36
F4	515	39
F5	555	39
F6	590	40
F7	630	50
F8	680	52
NIR(Near IR)	910	n/a
Clear	Si response/non filtered	n/a
FD(Flicker Detection)	Si response/non filtered	n/a

Table 4.5: AS7341 Optical Channel.

Figure 4.28 shows a MATLAB simulation comparing the spectral response of the mini spectrometer with discrete channels to that of the Avantes spectrometer. The results indicate that each channel of the cost-effective mini spectrometer provides an adequate response relative to the corresponding measurements from the Avantes spectrometer.

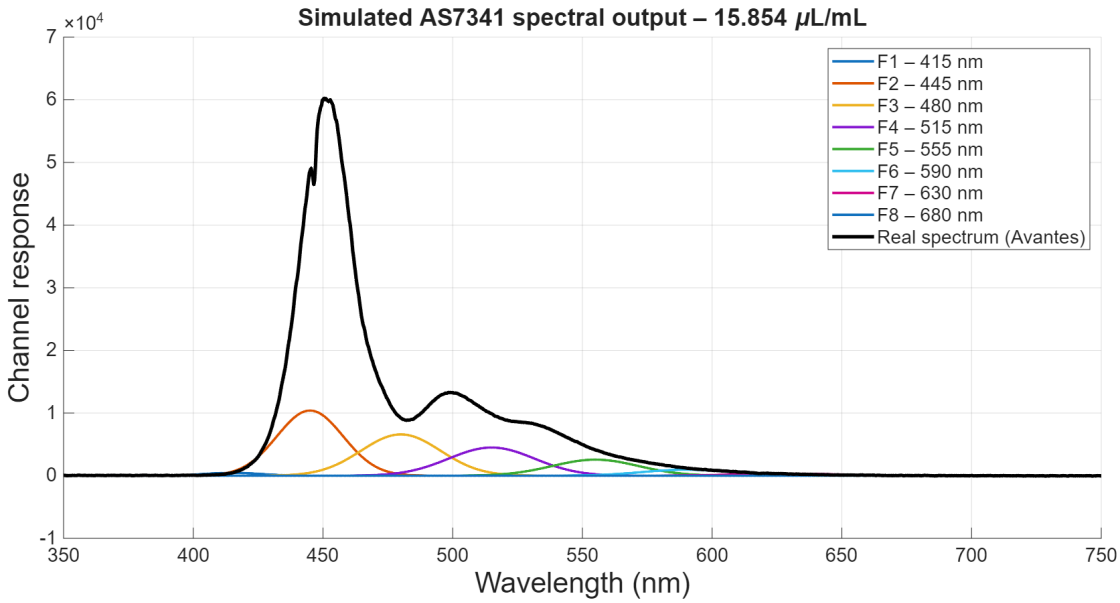

Figure 4.28: Spectral response of mini-spectrometer Adafruit AS7341.

4.7 PCB Layout

Based on the predefined board dimensions and mechanical placement constraints, the PCB layout was designed within the CAD environment by positioning connectors, buttons/switches, screw holes, assembly holes, and other required mechanical elements. This phase is referred to as the PCB structural design.
Subsequently, the electronic components were placed on the board according to the following principles:

1. The layout was reasonably partitioned according to electrical performance, generally separating the board into: digital circuit areas (susceptible to interference and capable of generating interference), analog circuit areas (sensitive to interference), and power supply areas (a potential source of interference).

2. Components performing the same function were placed as close as possible to each other and arranged to ensure the simplest possible interconnections. Furthermore, the relative positions of the functional blocks were adjusted to simplify signal routing between them.

3. I/O driver components were placed close to the edge of the board and near the corresponding connectors.

4. A decoupling capacitor was placed between the power supply input pin and ground pin of each integrated circuit (typically a high-frequency ceramic capacitor). For highly populated circuits, the addition of tantalum capacitors distributed around groups of integrated circuits was also considered.

5. The overall layout was kept balanced and orderly, avoiding excessive crowding on the top layer and preventing disorganized component placement.

After this phase, the routing stage was carried out. Routing represents a critical step in the entire PCB design process, as it directly affects the overall performance of the board.
Following the optimization of the routing and the silkscreen layer, the design rules were selected to keep the prototype manufacturing cost low. The following figures illustrate the PCB layout of the main board, which includes the MCU and the associated circuitry (figure 4.30), and the LED board (figure 4.29), which integrates the four LEDs. Furthermore, the measurement setup is shown (figure 4.31), consisting of the enclosure housing the cuvette, the AS7341 mini spectrometer, and the LED board.

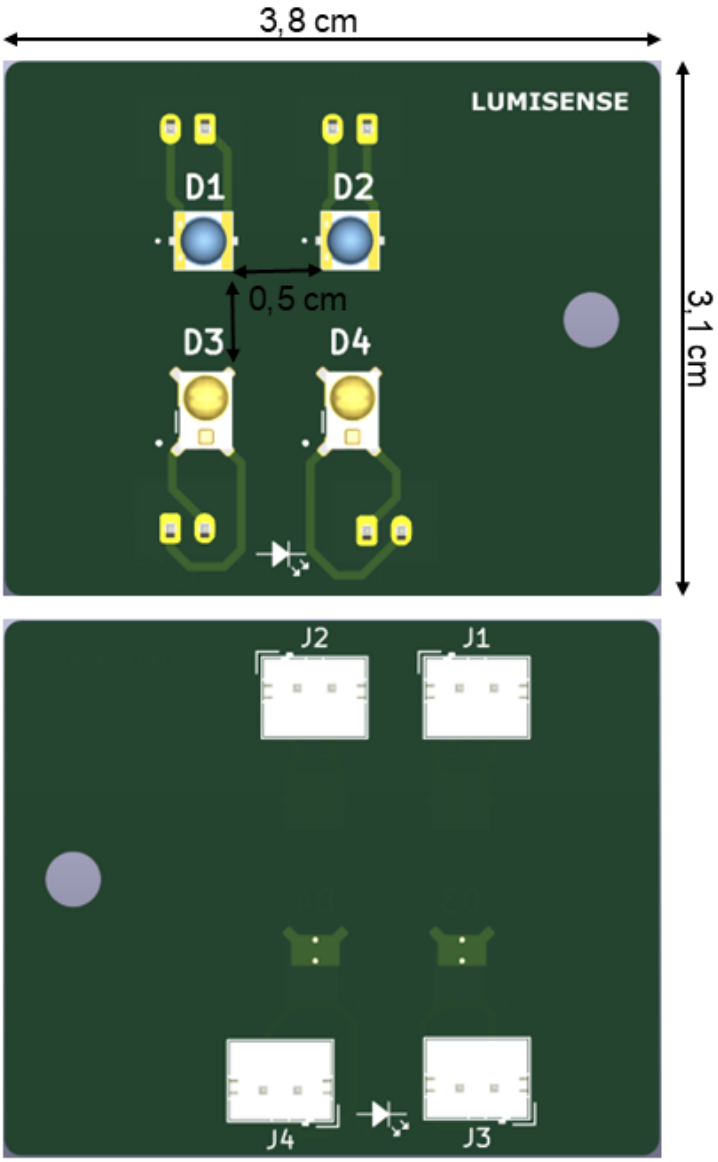

Figure 4.29: Led board.

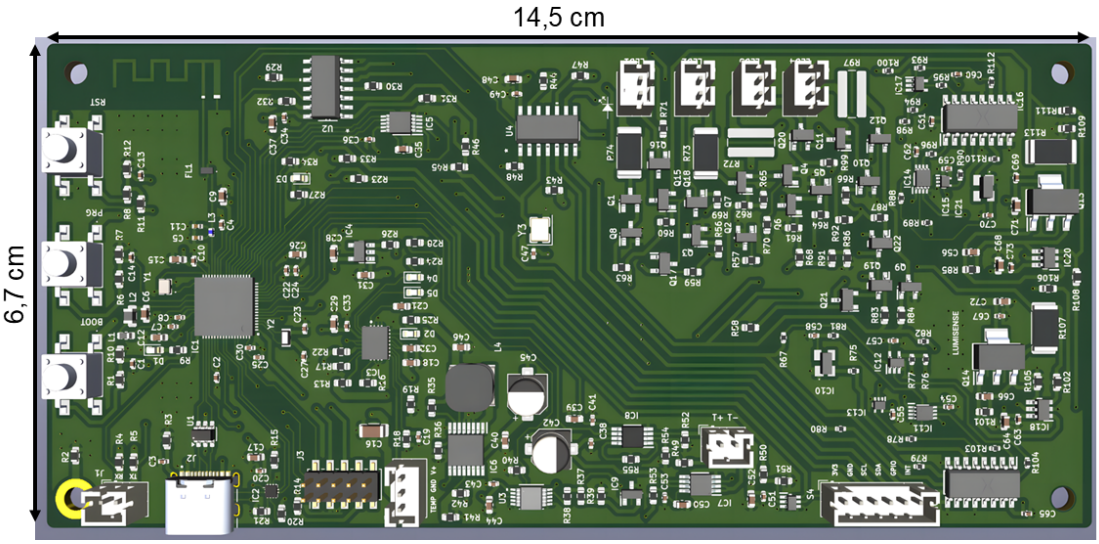

Figure 4.30: Main board.

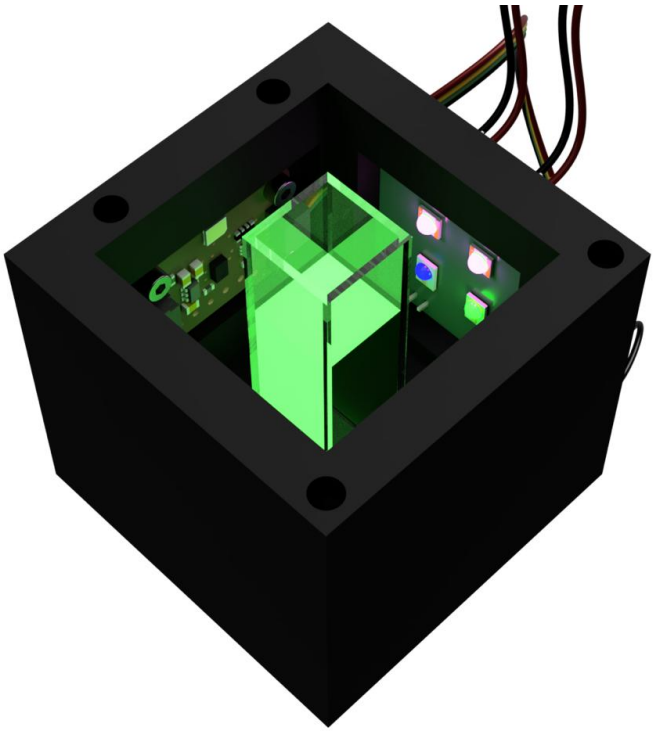

Figure 4.31: Cuvette holder with led board on the right side of the image and Adafruit AS7341 on the left side.

Chapter 5

Firmware configuration

The firmware was developed using the STM32CubeIDE and STM32CubeMX software environments[15]. In the initial phase, the microcontroller pins were configured in STM32CubeMX according to the schematic designed in KiCad. This step allowed each pin to be assigned its specific function required by the project, as illustrated in the corresponding figure 5.1. The table 5.1 below provides a detailed description of each component associated with the respective pins.

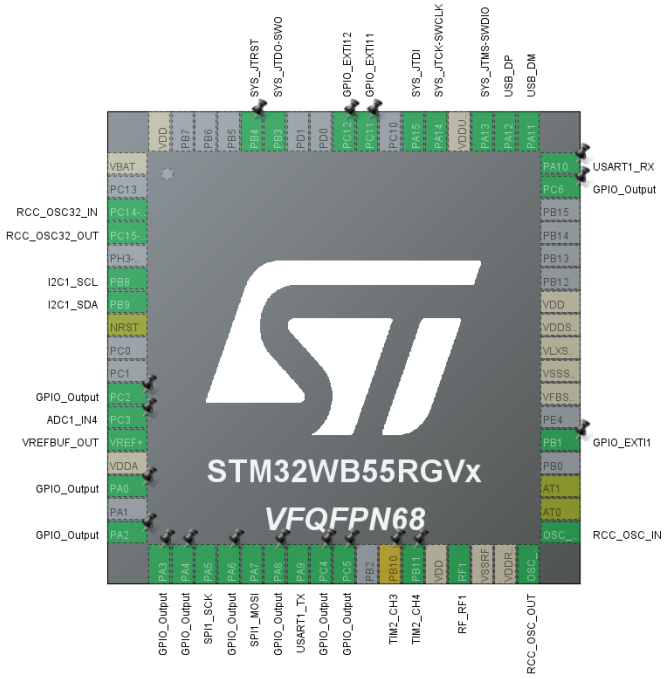

Figure 5.1: Pinout view of STM32WB55RGVx.

Component	Port	Configuration	Description
RCC_OSC32_IN	PC14	Oscillator	Input oscillator 32 kHz
RCC_OSC32_OUT	PC15	Oscillator	Output oscillator 32 kHz
I2C1_SCL	PB8	I2C bus	Provides the serial clock for the I2C1 bus
I2C1_SDA	PB9	I2C bus	Carries the bidirectional data signal
GPIO_OUT	PC2	3.3 V output	Activate instrumentation amplifier for NTC acquisition
ADC1_IN4	PC3	Single-ended ADC	NTC temperature acquisition
VREFBUF_OUT	VREF+	2.048 V output	Delivers a stable reference voltage to the ADC
GPIO_OUT	PA0	3.3 V output	GPIO connection to AS7431 mini-spectrometer
GPIO_EXTI1	PA1	External interrupt	AS7431 mini-spectrometer interrupt
GPIO_OUT	PA2	3.3 V output	Activate AS7431 mini-spectrometer power supply
GPIO_OUT	PA3	3.3 V output	PCB LED1 output
GPIO_OUT	PA4	3.3 V output	GPIO connection to DAC ($\overline{LDAC}$ pin)
SPI1_SCK	PA5	Clock SPI1	Serial clock to DAC (SCLK pin)
GPIO_OUT	PA6	3.3 V output	GPIO connection to DAC ($\overline{SYNC}$ pin)
SPI1_MOSI	PA7	MOSI SPI1	Serial data output to DAC (D_{IN})
GPIO_OUT	PA8	3.3 V output	GPIO connection to D-FF
USART1_TX	PA9	UART	UART1 transmission
GPIO_OUT	PC4	3.3 V output	GPIO connection to D-FF
GPIO_OUT	PC5	3.3 V output	GPIO connection to D-FF
TIM2_CH3	PB10	PWM generation	PWM for LED1 and LED2
TIM2_CH4	PB10	PWM generation	PWM for LED3 and LED4
RF_RF1	RF1	RF module	Antenna RF output (BLE/Thread/Zigbee)
RCC_OSC_OUT	OSC-OUT	Oscillator	Output oscillator 32 MHz
RCC_OSC_IN	OSC-IN	Oscillator	Output oscillator 32 MHz
GPIO_OUT	PC6	3.3 V output	PCB LED2 output
GPIO_EXTI1	PB1	External Interrupt	Hardware input button
USART1_RX	PA10	UART	UART1 reception
USB_DM	PA11	Data line	Differential data line for USB signal's negative phase
USB_DP	PA12	Data line	Differential data line for USB signal's positive phase
SYS_JTMS-SWDIO	PA13	SWDIO / JTAG	Debugging SWD / JTAG interface
SYS_SWCLK	PA14	SWCLK / JTAG	Debugging SWCLK / JTAG interface
SYS_JTDI	PA15	JTDI / AF	JTAG input
GPIO_EXTI11	PC11	External Interrupt	GPIO for USBC port controller
GPIO_EXTI12	PC12	External Interrupt	GPIO for USBC port controller
SYS_JTDO-SWIO	PB3	JTDO / SWO	JTAG / SWO output
SYS_JTRST	PB4	JTRST	JTAG reset input

Table 5.1: Port configuration of the STM32 MCU.

5.1 Program flow

The figure 5.2 illustrates a simplified state flow of the custom PCB. The system enters the programming state when the BOOT button is pressed during the startup process, whereas pressing the RESET button during whatever phase of the execution triggers a system reset by generating a high priority interrupt. At startup, if neither button is pressed, the system proceeds with the USB-C port controller

setup, during which two GPIO pins are configured to set the output current.
Following this, the system enters the idle state, where GPIO_SEL_OUT_2 is set to a logic high (1), selecting PWM mode while the DAC is disabled, keeping the entire LED circuitry turned off (as no square wave is provided the duty cycle is 0%).
When an operational change is requested, the system transitions to the `SETUP_MODE`. In this state, the system receives commands via the COM port. Only two commands are considered valid: `SETHP:X;Y` and `SETPWM:X;Y`. Any other command prompts the system to request a valid command.
When the `SETHP` command is inserted, the Howland Pump is selected, and the integer values X and Y determine which LEDs are activated via GPIO_SEL_OUT_1 and GPIO_SEL_OUT_3. The system then moves to the `EMISSION_MODE_HP` state, where it requests a valid DAC configuration through the COM port to provide a voltage setpoint for the Howland Pump. This is achieved through the command `SETDAC:X;Y`, where `X` specifies the DAC channel and `Y` determines the output value. From the emission state, the system can be stopped, returning to the `IDLE_STATE`. The same operational logic applies to PWM mode, following analogous commands and state transitions. When the system enters the `EMISSION_MODE_PWM` state, it requires the command `SETDUTY:X;Y`, where `X` selects PWM_OUT_1 or PWM_OUT_2, and `Y` specifies the duty cycle value. In this case a valid percentage for the duty cycle can be provided to dynamically change the LED emission level.

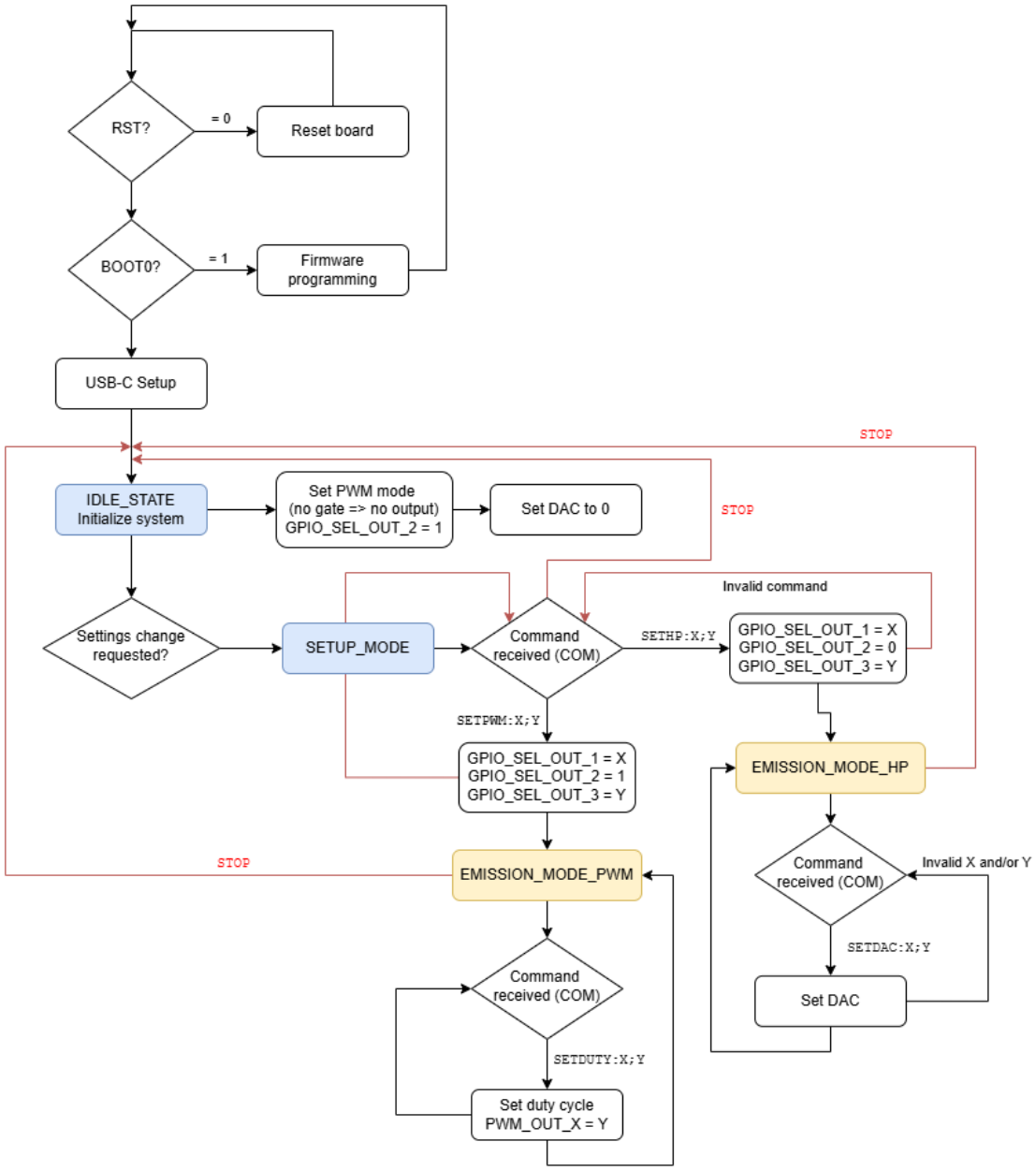

Figure 5.2: Execution flow of the system.

5.2 Program flow of the DAC

The DAC7562 features a three-wire serial interface consisting of SYNC, SCLK, and DIN [27].The input shift register of the DAC7562 is 24 bit wide and is structured in table 5.2.
All 24 bits are loaded into the DAC shift register under the control of the serial clock (SCLK). The most significant bit (DB23) is transmitted first, followed by the remaining bits of the 24 bit word in a left-aligned sequence. Consequently, only the first 24 bit clocked into the device are latched into the shift register; any additional clock pulses are ignored.
A write operation begins when the SYNC line is driven low. Data present on DIN are shifted into the 24 bit register on each falling edge of SCLK. The serial clock can operate at frequencies up to 50 MHz.
On the 24th falling edge of SCLK, the final data bit is loaded and the shift register is locked. Additional clock pulses do not modify the stored data. Immediately after the 24th falling edge, the DAC7562 decodes the command bits, address bits, and data bits to execute the requested operation; this occurs without waiting for a rising edge on SYNC.
After the 24th falling edge of SCLK, the SYNC line may either remain low or return high. However, the minimum delay between the 24th falling edge of SCLK and the next falling edge of SYNC must be respected to ensure proper initiation of the subsequent write cycle.
If SYNC rises before the 24 bit sequence is completed, the SPI interface is reset and the data transfer is aborted. A new write cycle can then begin at the next falling edge of SYNC.
When writing to the DAC input registers, the 16, 14, or 12 data bits that follow are interpreted by the device to generate the corresponding analog output voltage. The data format is straight binary, where all zeros correspond to a 0 V output and all ones correspond to full-scale output. For documentation purposes, the data representation is described using a true 16 bit format (i.e., FFFFh corresponds to full-scale output), which is the format required by the DAC7562 device. Figure 5.3 show the simplified program flow the Digital-to-Analog converter.

Bit	Field Name	Description	Default Value
23-22	DB23-DB22	DB23(MSB)	X
21	C2(DB21)	Command bit	0/1
20	C1(DB20)	Command bit	0/1
19	C0(DB19)	Command bit	0/1
18	A2(DB18)	Address bit	0/1
17	A1(DB17)	Address bit	0/1
16	A0(DB16)	Address bit	0/1
15	DB15	Data bit (D11)	X
14	DB14	Data bit (D10)	X
13	DB13	Data bit (D9)	X
12	DB12	Data bit (D8)	X
11	DB11	Data bit (D6)	X
10	DB10	Data bit (D5)	X
9	DB9	Data bit (D4)	X
8	DB8	Data bit (D3)	X
7	DB7	Data bit (D2)	X
6	DB6	Data bit (D1)	X
5	DB5	Data bit (D0)	1
4	DB4	Power-up DAC-A and DAC-B	0
3	DB3	Don't care bit	X
2	DB2	Don't care bit	X
1	DB1	DAC-B uses $\overline{LDAC}$ pin	0
0	DB0(LSB)	DAC-A uses $\overline{LDAC}$ pin	0

Table 5.2: Data input register format.

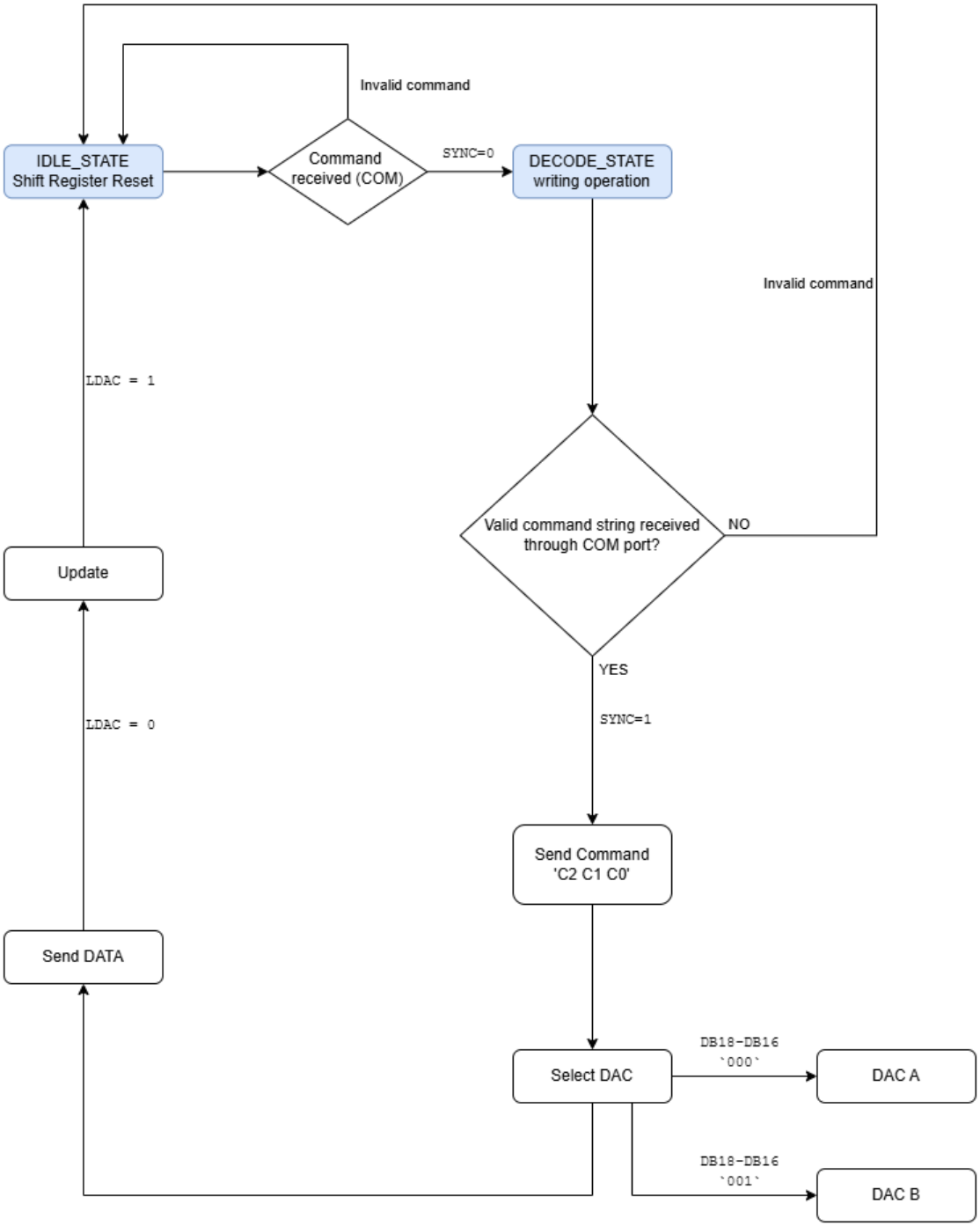

Figure 5.3: Simplified execution flow of the DAC.

Chapter 6

Conclusions

This thesis presented the development of a low-cost, portable prototype for water quality monitoring based on fluorescence methodologies. The system integrates a mini-spectrometer with a matrix of programmable LEDs, enabling controlled optical excitation and reliable spectral detection. The device, battery-powered, is designed for field use and deployment in remote locations, ensuring precise sample temperature detection and stable light emission through a dedicated LED driving circuit.

Regarding future perspectives, a more comprehensive characterization of the prototype is necessary. First, the electronic board must be thoroughly tested to verify the correct operation of all components and ensure overall reliability. Targeted experiments using fluorescent microspheres with LEDs of different wavelengths are also planned and supported by the prototype. Simultaneously, it will be essential to analyze the influence of different LED driving methods, such as the Howland current pump or PWM control, on the discrete measurements provided by the AS7341 mini-spectrometer, as well as to assess the impact of physical phenomena such as photobleaching or quenching on the reproducibility of results. Additionally, the implementation of machine learning algorithms (developed by colleague Flavia Tarantino) is foreseen for advanced data processing using the mini-spectrometer's discrete readings. Finally, accurately estimating the device's limit of detection (LOD) and expanding experimental trials to include real bacterial samples will be critical for validating the system in practical and realistic application scenarios.

List of Figures

1.1 Jablonski diagram illustrating the processes involved in the creation of an excited electronic singlet state by optical absorption and subsequent emission of fluorescence[1]. 4
1.2 (a) Idealized potential energy curve for a diatomic molecule. In general, polyatomic molecules will have $3N-6$ vibrational modes (ν_1, ν_2, ν_3,..), where N is the number of atoms, and will be asymmetric rotors with three different inertial axes. (b) Morse potentials for a molecule in the singlet ground state S_0 and first excited singlet state S_1 to demonstrate the Franck–Condon principle [2]. 6
1.3 A simplified Jablonski diagram to illustrate the meaning of quantum yields and lifetimes[4]. 7
1.4 Excitation of a fluorophore at three different wavelengths (EX 1, EX 2, EX 3) does not change the emission profile but does produce variations in fluorescence emission intensity (EM 1, EM 2, EM 3) that correspond to the amplitude of the excitation spectrum[1]. . . 9

2.1 Schematic of bacterial detection: Bacteria are fixed on glass slides, permeabilized to allow entry of a PNA probe labeled with Alexa Fluor 488, which binds specific rRNA regions. After washing, only the targeted bacteria remain fluorescent and can be imaged with the smartphone microscope[5]. 13
2.2 a)Schematic of the DLS-based system used in the experiments. b)Detail showing fiber collecting scattered light[6]. 15
2.3 a)Signals of water. b)Zoomed-in version of a). c)Number of events detected by our system in 10 min for different concentrations of virus particles[6]. 15

3.1 Illustration of the measurement concept. 17
3.2 T-Cube LED Driver [7]. 17
3.3 M450LP2 mounted LED [8]. 17
3.4 Avantes Spectrometer LED [9]. 18

3.5 Spectra captured by the laboratory spectrometer. 19
3.6 Illustration of the intensity variation. 19
3.7 Quadratic interpolation. 20
3.8 Illustration of the measurement concept. 21
3.9 UV Led SMD Wurth Elektronik[11]. 22
3.10 LUXEON Rebel Color single color Led SMD [12]. 22
3.11 Irradiance of single LEDs (LED array). 24
3.12 Total irradiance of the LED array (the circles represent the positions of the various LEDs, while the vertical lines the position of the cuvette). 25
3.13 Irradiance of single leds (LED matrix). 26
3.14 Total irradiance of the LED matrix (the circles represent the positions of the various LEDs, while the vertical lines the position of the cuvette). 27
3.15 Combined irradiance of the LED matrix(LED 1+LED2; LED1+LED3). 28
3.16 Combined irradiance of the LED matrix(LED 1+LED4; LED2+LED3). 28
3.17 Combined irradiance of the LED matrix(LED 2+LED4; LED3+LED4). 29

4.1 Four-layer PCB stack-up [14]. 30
4.2 Schematic in KiCad of the MCU. 32
4.3 USB Type-C® connector pins[16]. 34
4.4 USB Type-C® design. 36
4.5 LDO and Battery charging circuitry. 37
4.6 Short current loop. 39
4.7 Power-Path Management. 39
4.8 Boost converter. 44
4.9 Led diode constant-current driver-1 circuit diagram. 45
4.10 The Howland pump. 46
4.11 Output current versus input voltage with +5 V supply. 48
4.12 Q_1 power dissipation versus input voltage with +5 V supply. 49
4.13 Led driver transient response with +5 V supply. 49
4.14 Led diode constant-current driver-2 circuit diagram. 50
4.15 Output current versus input voltage with +3.3 V supply. 51
4.16 Q_1 power dissipation versus input voltage with +3.3 V supply. . . . 51
4.17 Led driver transient response with +3.3 V supply. 52
4.18 PWM duty cycle [23]. 52
4.19 Schematic of the switching circuit for LED and power supply selection (Howland pump or PWM). 54
4.20 Two dual-channel D-type flip-flops. 57
4.21 Digital-to-analog converter. 58
4.22 Howland pump with enable pin. 59
4.23 Security Circuitry. 60

4.24 Timing diagram of security circuit. 60
4.25 Temperature sensing circuit. 62
4.26 Temperature acquisition circuit. 64
4.27 Adafruit AS7341 10-Channel Light[10]. 66
4.28 Spectral response of mini-spectrometer Adafruit AS7341. 67
4.29 Led board. 69
4.30 Main board. 70
4.31 Cuvette holder with led board on the right side of the image and Adafruit AS7341 on the left side. 70

5.1 Pinout view of STM32WB55RGVx. 71
5.2 Execution flow of the system. 74
5.3 Simplified execution flow of the DAC. 77

List of Tables

3.1 LED characteristics. 21

4.1 OUT1 e OUT2 pin settings. 35
4.2 A 2 mA current source and its internal behavior for different values of v_L(a negative current indicates that the current flows in the direction opposite to the arrow). 47
4.3 Specifications MOSFET. 55
4.4 Control signal combinations and transistor states. 56
4.5 AS7341 Optical Channel. 66

5.1 Port configuration of the STM32 MCU. 72
5.2 Data input register format. 76

Acknowledgements

I would like to dedicate this thesis to my grandmother, Rosa, my angel in heaven, who continues to watch over me from above and whose presence will always remain in my heart.

A special thanks goes to my girlfriend, Flavia, who has stood by my side throughout these intense years of study. With her constant support, patience, and encouragement, she helped me face the many challenges along this journey. Together we overcame numerous difficulties and celebrated every achievement along the way.

I would also like to express my heartfelt gratitude to my family, my father, mother, brother, and sister, for always believing in me and supporting me throughout my academic path. Their advice, encouragement, and unconditional trust have been fundamental in helping me reach this important milestone.

My sincere gratitude also goes to Professor Guido Perrone for his guidance, availability, and for giving me the opportunity to undertake this research project, which represents a significant step in my academic journey.

I am also deeply grateful to Chiara Bellezza Prinsi and Leonardo Degl'Innocenti for their invaluable support and guidance throughout the development of this work.

Finally, I would like to thank Alite SRL for welcoming me into their company and giving me the opportunity to carry out my thesis project within their organization, allowing me to gain valuable professional and personal experience.

Bibliography

[1] Thermo Fisher Scientific. *Introduction to Fluorescence Techniques*. https://www.thermofisher.com/it/en/home/references/molecular-probes-the-handbook/introduction-to-fluorescence-techniques.html. Section from the *Molecular Probes Handbook – A Guide to Fluorescent Probes and Labeling Technologies*, a comprehensive guide to fluorescent probes and detection techniques. 2026 (cit. on pp. 3, 4, 8, 9).

[2] Markus. Sauer, Johan. Hofkens, and J.. Enderlein. *Handbook of fluorescence spectroscopy and imaging : from single molecules to ensembles*. Wiley-VCH, 2011, p. 281. ISBN: 9783527316694 (cit. on pp. 5, 6).

[3] PerkinElmer Ltd. *An Introduction to Fluorescence Spectroscopy*. User assistance manual; printed copy at Post Office Lane, Beaconsfield, Buckinghamshire HP9 1QA. PerkinElmer Ltd. Beaconsfield, Buckinghamshire, UK, 2000. URL: https://www.chem.uci.edu/~dmitryf/manuals/Fundamentals/Fluorescence%20Spectroscopy.pdf (cit. on pp. 6, 9).

[4] «Introduction to Fluorescence». In: *Principles of Fluorescence Spectroscopy*. Ed. by Joseph R. Lakowicz. Boston, MA: Springer US, 2006, pp. 1–26. ISBN: 978-0-387-46312-4. DOI: 10.1007/978-0-387-46312-4_1. URL: https://doi.org/10.1007/978-0-387-46312-4_1 (cit. on pp. 7, 12).

[5] Vilhelm Muller, Jose M. Sousa, Hatice Ceylan Koydemir, Muhammed Veli, Derek Tseng, Laura Cerqueira, Aydogan Ozcan, Nuno F. Azevedo, and Fredrik Westerlund. «Identification of pathogenic bacteria in complex samples using a smartphone-based fluorescence microscope». In: *RSC Advances* (2018) (cit. on p. 13).

[6] Anish Dahal, Shishir Gurung, Avash Kattel, Rijan Maharjan, Jack Radford, Philip Binner, Ilya Starshynov, Daniele Faccio, and Ashim Dhakal. *Low-cost Dynamic Light Scattering to Detect Rotavirus Particles in Drinking Water*. Tech. rep. URL: www.unicef.org/wash (cit. on pp. 14, 15).

[7] Thorlabs. *T-Cube texttrademark LED Driver: LEDD1B*. T-Cube Series LED Driver designed for high-power LEDs; max output current 1200 mA. Thorlabs, Inc. Newton, NJ, USA, 2018. URL: https://www.thorlabs.com/item/LEDD1B (cit. on pp. 16, 17).

[8] Thorlabs. *Mounted LED, 450 nm (Royal Blue): M450LP2*. High-power 450 nm mounted LED with approx. 2118 mW minimum output, 120° viewing angle, and 2000 mA max drive current. Thorlabs, Inc. Newton, NJ, USA, 2024. URL: https://www.thorlabs.com/mounted-leds?pn=M450LP2 (cit. on pp. 16, 17, 21).

[9] Avantes BV. *AvaSpec-3648 Fiber Optic Spectrometer*. High-resolution fiber optic spectrometer based on a 75 mm Czerny-Turner optical bench with a 3648-pixel CCD detector, USB2.0 interface, and wide spectral range; includes AvaSoft software and interface cable. Avantes BV. Apeldoorn, Netherlands, 2024. URL: https://www.avantes.ru/en/spectrometer/avaspec3648.php (cit. on pp. 16, 18).

[10] Bryan Siepert and Kattni Rembor. *Adafruit AS7341 10-Channel Light / Color Sensor Breakout – Overview*. https://learn.adafruit.com/adafruit-as7341-10-channel-light-color-sensor-breakout/overview. Adafruit Learning System, published August 13, 2020, updated January 22, 2025. Adafruit, 2020. URL: https://learn.adafruit.com/adafruit-as7341-10-channel-light-color-sensor-breakout/overview (cit. on pp. 20, 66).

[11] Würth Elektronik. *WL-SUMW SMT Ultraviolet LED, 365 nm (Part No. 15335337AA350)*. Product datasheet and specifications. High-power UV-A LED, 365 nm wavelength, surface mount (SMD/SMT) package, typical forward voltage 3.8 V and forward current 500 mA. 2025. URL: https://www.mouser.it/ProductDetail/Wurth-Elektronik/15335337AA350?qs=sPbYRqrBIVmHWH%252Bm%2FfGWUQ%3D%3D (cit. on pp. 21, 22).

[12] Lumileds Holding B.V. *LUXEON Rebel Color Blue LED, LXML / PB01-0040*. Product datasheet and specifications. Single-color high power blue SMD LED, dominant wavelength 470 nm, typical forward voltage 2.95V, typical luminous flux 40lm at 350mA forward current; surface mount package. 2025. URL: https://www.mouser.it/ProductDetail/Lumileds/LXML-PB01-0040?qs=7Vwje68bFtNkkjiJ6snd6g%3D%3D (cit. on pp. 21, 22).

[13] Vasiliki Naskari, Gregory Doumenis, and Ioannis Masklavanos. «Irradiance Non-Uniformity in LED Light Simulators». In: *Information* 14.6 (2023). ISSN: 2078-2489. DOI: 10.3390/info14060316. URL: https://www.mdpi.com/2078-2489/14/6/316 (cit. on p. 23).

[14] Alice Lee. *Guida alla progettazione di PCB a 4 strati: stackup e best practice*. https://www.globalwellpcba.com/it/progettazione-pcb-a-4-strati/. Ultimo aggiornamento: 11 giugno 2025; guida online sulla progettazione di circuiti stampati a 4 strati, incluse configurazioni standard di stackup, vantaggi, pratiche di progettazione e applicazioni comuni. June 2025 (cit. on p. 30).

[15] STMicroelectronics. *STM32WB55RG - Multiprotocol wireless 32-bit MCU Arm Cortex-M4 with Bluetooth 5 and 802.15.4*. 2026. URL: https://www.st.com/en/microcontrollers-microprocessors/stm32wb55rg.html (cit. on pp. 31, 71).

[16] Digi-Key Electronics and Contributors. *Designing in USB Type-C and Using Power Delivery for Rapid Charging*. Digi-Key Electronics. Mar. 2017. URL: https://www.digikey.com/en/articles/designing-in-usb-type-c-and-using-power-delivery-for-rapid-charging (cit. on pp. 33, 34).

[17] Texas Instruments. *TUSB320 USB Type-C Configuration Channel Logic and Port Control*. https://www.ti.com/product/TUSB320. Datasheet and product information; USB Type-C CC logic controller supporting DFP/UFP/DRP configurations, CC detection, and up to 3A current advertisement. 2022 (cit. on p. 34).

[18] STMicroelectronics. *Basics of Power Supply Design for MCU (Under Voltage Lockout – UVLO)*. https://wiki.st.com/stm32mcu/wiki/Basics_of_power_supply_design_for_MCU#Under_voltage_lockout_(-UVLO-). STM32 MCU wiki, technical guide on power supply basics including UVLO. STMicroelectronics, 2025 (cit. on p. 37).

[19] Texas Instruments. *TPS7A20 300mA Ultra-Low-Noise, Low-IQ, High PSRR LDO Linear Regulator*. https://www.ti.com/product/TPS7A20. Product information and datasheet; low-noise, high PSRR low-dropout linear regulator. Texas Instruments, 2024 (cit. on p. 38).

[20] Texas Instruments. *BQ24070 1-Cell 2 A Li-Ion Linear Battery Charger and Power-Path Management IC*. https://www.ti.com/product/BQ24070. Product information and datasheet for the BQ24070 single-chip Li-Ion charge and system power-path management device. Texas Instruments, 2025 (cit. on p. 39).

[21] Texas Instruments. *TPS61032 5-V Output, 1-A, 96% Efficient Synchronous Boost Converter*. https://www.ti.com/product/TPS61032. Product page and datasheet for the TPS61032 boost DC–DC converter. Texas Instruments, 2015 (cit. on p. 42).

[22] Neil P. Albaugh. *Optoelectronics Circuit Collection*. Application Report SBEA001. Texas Instruments. Dallas, TX, USA, Sept. 2001. URL: https://www.ti.com/lit/an/sbea001/sbea001.pdf (cit. on p. 45).

[23] Martin Van. *Controllo LED efficiente: esplorazione dell'attenuazione PWM*. https://www.ledyilighting.com/it/led-pwm-dimming/. Mar. 2023 (cit. on p. 52).

[24] Yue Wang, Yile Fang, Haoran Liu, Xiangyi Su, Zhu Chen, Song Li, and Nongyue He. «A Highly Integrated and Diminutive Fluorescence Detector for Point-of-Care Testing: Dual Negative Feedback Light-Emitting Diode (LED) Drive and Photoelectric Processing Circuits Design and Implementation». In: *Biosensors* 12.9 (2022). ISSN: 2079-6374. DOI: 10.3390/bios12090764. URL: https://www.mdpi.com/2079-6374/12/9/764 (cit. on p. 53).

[25] Diodes Incorporated. *DMG3401LSN: 30 V P-Channel Enhancement Mode MOSFET*. Datasheet and technical specifications. Diodes Incorporated. Plano, TX, USA, 2026. URL: https://www.diodes.com/part/view/DMG3401LSN (cit. on p. 55).

[26] Vishay Siliconix. *SI2304DDS: N-Channel 30 V (D-S) MOSFET Datasheet*. Document No. 65175, Rev. A, 10-Aug-2009. Vishay Intertechnology, Inc. Malvern, PA, USA, Aug. 2009. URL: https://www.vishay.com/docs/65175/si2304dds.pdf (cit. on p. 55).

[27] Texas Instruments. *DAC7562 – 12-Bit Dual Low-Power Buffered Voltage-Output DAC*. Datasheet and product information available online. Texas Instruments. Dallas, TX, USA, 2015. URL: https://www.ti.com/product/DAC7562 (cit. on pp. 58, 75).